Alma Mater Studiorum - Università di Bologna

SCUOLA DI SCIENZE

Dipartimento di Chimica Industriale “Toso Montanari”

Corso di Laurea Magistrale in

Chimica Industriale

Classe LM-71 - Scienze e Tecnologie della Chimica Industriale

Development and characterization of bismuth carbon-integrated electrocatalysts for high-temperature electroreduction of CO_2 to formic acid

Tesi di laurea sperimentale

CANDIDATO

Giovanni Berluti

RELATORE

Chiar.mo Prof. Patricia Benito Martin

CORRELATORE

Alana Rossen

Anno Accademico 2022-2023

Abstract

Nowadays global warming is the biggest challenge the human species has to face. Greenhouse gas emissions from anthropogenic activity, of which carbon dioxide occupies the largest share, are the main cause of climate changes observed in the last century. Carbon capture and utilisation (CCU), is one of the most promising prospects to combat this problem. With this approach, carbon dioxide can be captured and separated from the different gaseous components, to be converted into different valuable chemical products, and re-introduced into the chemical market, adopting the circular economy principle. One of the most advanced pathways to convert CO_2 is by using green current to reduce it into different chemicals. The use of electrolysers to supply electrons to the carbon dioxide stream and reduce it electrochemically to small molecules, such as formic acid and carbon monoxide, which is considered one of the best options from an economic point of view, has been studied and will be explained in this paper. The conversion of carbon dioxide by electrochemical reduction requires the use of several components within the electrolyser to improve the selectivity and yield of the process.

Electrocatalysts are the key components to promote these factors.

The use of an electrocatalyst is crucial to fragment the thermodynamic barrier of the process and make it feasible by improving the kinetics, increasing the selectivity towards the desired product, and limiting the waste of current leading to co-products. Over the years, various electrocatalysts have been studied to promote the process and, depending on the target product, different classes have been adopted.

For example, the electrocatalytic reduction of CO_2 to formic acid is usually catalysed by bismuth or tin, which have the highest selectivity.

The electroreduction of CO_2 can be coupled with different oxidation reactions, such as paraffin oxidation to olefins. When these types of counter-reactions are involved to make the overall process more convenient, the electrolyzer conditions, such as temperature and pressure, must be re-adjusted. The electroreduction of CO_2 at temperatures above room temperature has only been studied in recent years, and many studies have yet to be developed. In this work, a new series of bismuth electrocatalysts integrated with carbon microparticles was synthesized and characterized to carry out the electroreduction of CO_2 to formic acid at high temperatures. The new catalyst series claims to be structural more stable at the

conditions at which the electrolyzer needs to work, avoiding the particles sintering at high temperature after long exposure. This project aims to provide new information on the new series of bismuth electrocatalysts and their performance in the target process by studying their behaviour at high temperatures, different current densities and different process durations, and analysing their structural stability and selectivity.

Keywords

CCU	Carbon capture and utilisation
CCS	Carbon capture and storage
HER	Hydrogen evolution reaction
OER	Oxygen evolution reaction
GDE	Gas diffusion electrode
GDL	Gas diffusion layer
MPL	Microporous layer
CL	Catalyst layer
PTFE	Polytetrafluoroethylene
PBI	Polybenzimidazole
CO_2RR	CO_2 reduction reaction
WE	Working electrode
CE	Counter electrode
RE	Reference electrode
CO_2ER	CO_2 electro reduction
CEM	Cation exchange membrane
AEM	Anion exchange membrane
HOR	Hydrogen oxidation and evolution reaction
SEM	Scanning electron microscope
XRD	X-Ray diffraction
TGA	Thermogravimetric analysis
ICP-MS	Inductively coupled plasma – mass spectroscopy
CV	Cyclic voltammetry
LSV	Linear sweep voltammetry
OCP	Open circuit potential
ECSA	Electrochemical active surface area
DLC	Double layer capacitance
DCM	Differential capacitance measurement
FE	Faradaic efficiency

Summary

Chapter 1
Introduction to the electrochemical conversion of CO_2 to chemicals

The first chapter of this thesis will provide the basic knowledge in the CO_2 reduction process by electrocatalytic methods, to explain the theoretical principles behind the applied technologies, the causes that led to the development of these techniques, and the future goals.

1. Climate Change and Global Warming

Scientists have been talking about greenhouse gasses and global warming since two centuries ago when the phenomenon itself was not yet well defined. As early as the 19th century, experiments conducted suggested the effect of climate change due to anthropogenic carbon emissions, but the consequences were still not clear at that time. Arrhenius himself wrote in his publication "*Worlds in the making, the evolution of the universe*" (*1908): "*By the influence of the increasing percentage of carbonic acid in the atmosphere, we may hope to enjoy ages with more equable and better climates, especially as regards the colder regions of the Earth".

Much more data have been studied in recent years, and since the late 1950s, the scientific community has agreed on the drastic influence of CO_2 emissions by human activities.

The concentration of greenhouse gasses on earth has been monitored and has been shown to increase significantly from 300 ppm before the start of the first industrial revolution to over 400 nowadays, with an overall increase in global temperature between 1.0 and 1.2 °C according to the National Oceanographic and Atmospheric Administration (NOAA) [a].

Beginning with the 1997 "Kyoto Protocol", signed by U.S. President Bill Clinton, it is possible to identify the first countries seeking to collectively manage the influence of human activities on the climate. The agreement aimed to reduce the concentration of six different greenhouse gasses in 41 countries in the United States and the European Union, to 5.2 percent below the 1990s level.

In 2015, 197 different countries signed the "Paris Climate Agreement" with the intent to minimize their greenhouse gas emissions. The goal of the new agreement is to set the global warming limit at 2°C, which is considered the point of no return after which there will be a dramatic impact on human life in terms of ecosystems devastation such as rising sea levels, floods, wildfires, and drought, lack of fresh water and countless other issues with a real impact on many sectors of our society.

The current goal is set to stop global warming at 1.5°C and to achieve this, every country must limit the anthropogenic release of greenhouse gases into the atmosphere, primarily CO_2. Furthermore, the implementation of carbon mitigation and enhancement policies will enable faster recovery and cooling of the planet.

1.1 The European Green Deal

With the “European Green Deal”, the European Union aims to achieve zero net greenhouse gas emissions by 2050 with a set of energy, climate, transportation, and fiscal policies that will reduce net gas emissions by at least 55 percent by 2030. This strategy will also ensure the economic growth, well-being, and improved health of European citizens through the use of cleaner energy sources, the provision of greener industrial and transportation products, the application of a circular economy, and the creation of new job sectors [b].

1.1.1 The Horizon Europe

To accelerate the transition process and achieve the results set by the Green Deal by 2030, the European Union created “The Horizon Europe” [c], the key funding program for research and innovation that aims to improve research in five different areas:

- Adaptation to climate change
- Cancer
- Healthy oceans, seas coastal & inland waters
- Climate-neutral and smart cities
- Soil health and food

On climate change adaptation, the project aims to fund research to accelerate the green transition to a healthy and prosperous future within safe boundaries and scale-up solutions. To achieve the proposed results, modern society needs to focus on different aspects such as:

- Diversification of energy resources and transition from fossil fuel-based energy to renewable energy production pathways
- The transition from combustion-engine vehicles to vehicles powered by battery or fuel cells
- Capture and storage of CO_2 industrial waste gas

All these key factors will play a significant role in pursuing the European Green Deal goals and the Horizon project will make it feasible for the European research and development sector to achieve the goals in the short time window provided.

1.2 Carbon Capture and Utilisation (CCU)

One of the main strategies to mitigate and reduce global warming is to capture CO_2 from industrial exhaust gasses. The capture of CO_2 streams avoids emissions to the atmosphere by using different chemical adsorption technologies. The main difference between the methods is the type of sorbent used in the process: the more mature process relies on strong base liquid sorbent while the newest relies on solid amine. While the former allows a better capture and a harder final separation from the sorbent for the CO_2, the latter allows an easier final separation but higher costs of capture [1]. Carbon separation is always followed by different steps depending on the applied approach. As Figure 1 shows at the beginning of the CO_2 valorisation pathway, the captured CO_2 was long-term stored in geological formations and deep ocean waters. This method is defined as carbon capture and storage (CCS) and was initially adopted to remove CO_2 emissions from the atmosphere while maintaining the same fossil fuel consumption.

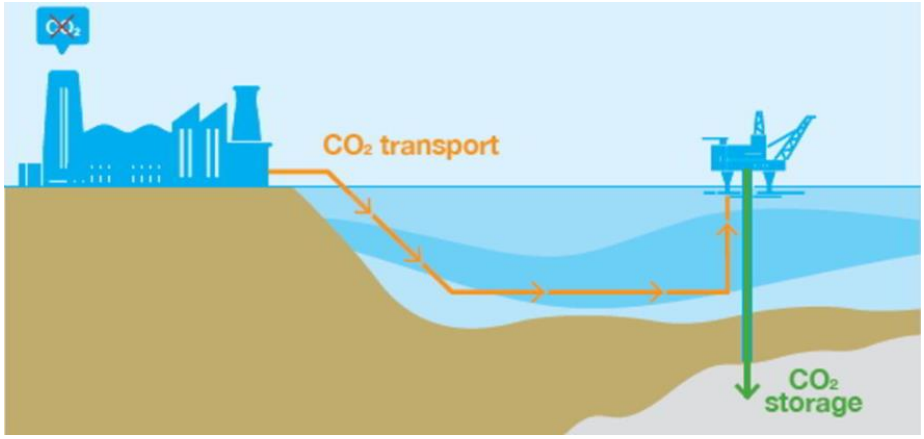

Figure 1 *CCS process diagram, Source: North Sea Transition Authority (NSTA).*

A different pathway may follow carbon capture such as the utilization of the sequestered CO_2 to produce new carbon-based products (Carbon capture and utilization CCU, Figure 2). The CCU pathway offers advantages over CCS, allowing what was considered a waste stream to be converted into valuable products reusable in the chemical market. Studies comparing CCS and CCU suggested that the former has greater mitigation potential, but the latter has better economic performance due to the additional profits from converting CO_2 into value-added chemical products [1].

A variety of carbon-based products can be obtained using different reaction pathways to utilize the sequestered CO_2; the most targeted are often carbon monoxide, syngas, methane, methanol, ethanol, formic acid, and ethylene. These building blocks will be

the source of a wide variety of chemicals, making the whole process economically feasible and respectful of the circular economy principles.

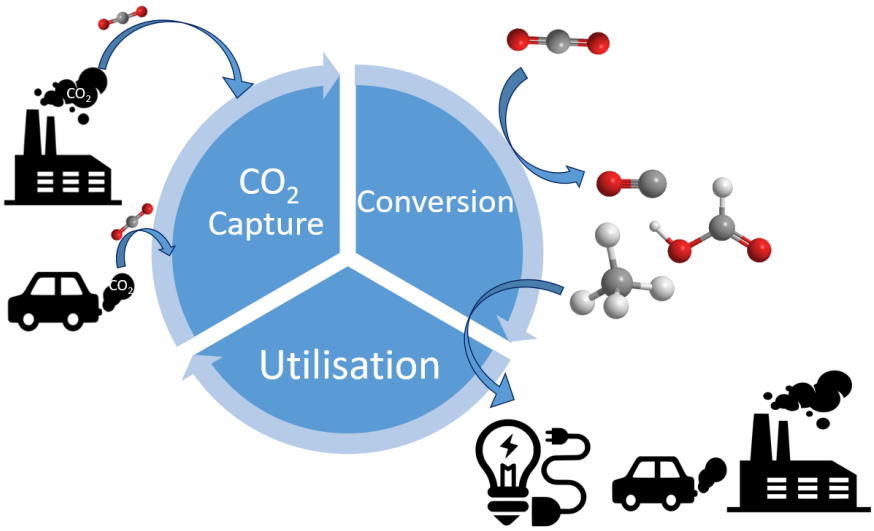

Figure 2 *CCU process diagram.*

A wide variety of reaction pathways can be found to convert CO_2 into other products, such as the hydrogenation reaction to produce methanol or carbon monoxide, the water gas shift reaction to produce hydrogen gas, and the Fischer Tropsch reaction to produce long-chain hydrocarbons.

Hydrogenation to methanol

$$CO_2 + 3H_2 \rightleftharpoons CH_3OH + H_2O \qquad \Delta H_r^0 = 49{,}3 \text{ kJ mol}^{-1}$$

Reverse water gas shift

$$CO_2 + H_2 \rightleftharpoons CO + H_2O \qquad \Delta H_r^0 = 41 \text{ kJ mol}^{-1}$$

Fischer Tropsch reaction

$$(2n+1)H_2 + nCO \rightleftharpoons C_nH_{2n+2} + nH_2O \qquad \Delta H_r^0 = -165 \text{ kJ mol}^{-1}$$

In recent years, one technology, in particular, has attempted to pursue the same goal with a completely green process and without the use of several chemical reagents, the electrochemical reduction of CO_2. This process involves the sole use of green electricity obtained from renewable sources and the CO_2 flow captured from industrial flue gasses or directly from the atmosphere.

1.3 CO_2 electrocatalytic reduction to chemicals

Electrocatalytic reduction of CO_2 consists in applying a constant current density to the cathode compartment of an electrolyzer at which, depending on the different catalysts

used, CO_2 will be reduced on the surface of the catalyst into different products depending on the number of electrons gained.

Table 1 *Electrochemical reduction pathways to different chemicals: 1-anion radical intermediate, 2-carbon monoxide, 3-formic acid, 4-methanol, 5-ethanol, [3].*

No.	Thermodynamic equilibrium half-reaction	Potentials V vs RHE
1	$CO_2 + e^- \rightarrow CO_2^{\bullet -}$	-1,49
2	$CO_2 + 2H^+ + 2e^- \rightarrow CO + H_2O$	-0,93
3	$CO_2 + 2H^+ + 2e^- \rightarrow HCOOH$	-1,07
4	$CO_2 + 6H^+ + 6e^- \rightarrow CH_3OH + H_2O$	-0,81
5	$CO_2 + 4H_2O + 6e^- \rightarrow CH_3CH_2OH + H_2O$	-0,74

The current density required to conduct the reduction is usually high because of the thermodynamic stability of the linear CO_2 molecule. The high potential needed can be a consistent disadvantage for the industrial feasibility of the project, as well as the low selectivity; on the other hand, the electrochemical reduction of carbon dioxide is an appealing method for both industrial and academic applications relying upon the following advantages [3]:

- It is easy to combine with renewable energy sources
- It will not generate CO_2 as a side product
- It has low cost and mild reaction conditions
- The reaction pathway can be easily controlled by changing the potential and current conditions
- By optimizing the catalyst, the reaction can be directed to the desired product with high selectivity, avoiding side products; in addition, the catalyst can be reused to reduce the overall chemical consumption

The CO_2 reduction competes with the hydrogen evolution reaction (HER) in a similar potential window depending on the catalyst used.

Hydrogen evolution reaction (HER)

$$H_2O + 2e^- \rightarrow H_2 + OH^- \qquad \Delta E^0 = -0{,}83 \text{ V Vs SHE}$$

Avoiding HER is critical to maximizing the selectivity of the process and can be done by optimizing the catalyst.

The type of catalyst can besides increase the selectivity, also influence the reaction potential needed, indeed using a catalyst with a minimized energy barrier can decrease the overall potential to be provided for the reaction.

Depending on the target product, different types of catalysts have already been tested and their performances evaluated, in particular, metal-based catalysts are famous for their high capabilities to produce several products already mentioned such as carbon monoxide, methane, formic acid, methanol, and ethylene. It is possible to divide this family of catalysts into three subcategories [4]:

- Transition metals such as Ag, Au, and Pt, are capable to generate carbon monoxide;
- Metals such as Sn, Pd, and Bi, can produce formic acid HCOOH as the main product;
- Cu is the only metal-based catalyst that can convert CO_2 to multi-carbon products and hydrocarbons.

Although the specific reaction mechanism for each product has not yet been discovered, experiments conducted in recent years suggested the existence of three main binding pathways that may diversify the type of final molecule obtained:

- Carbon hydrogenation
- Oxygen hydrogenation
- Carbon-carbon coupling

Depending on the type and order of these bonds, different pathways lead to several products as shown in Figure 3.

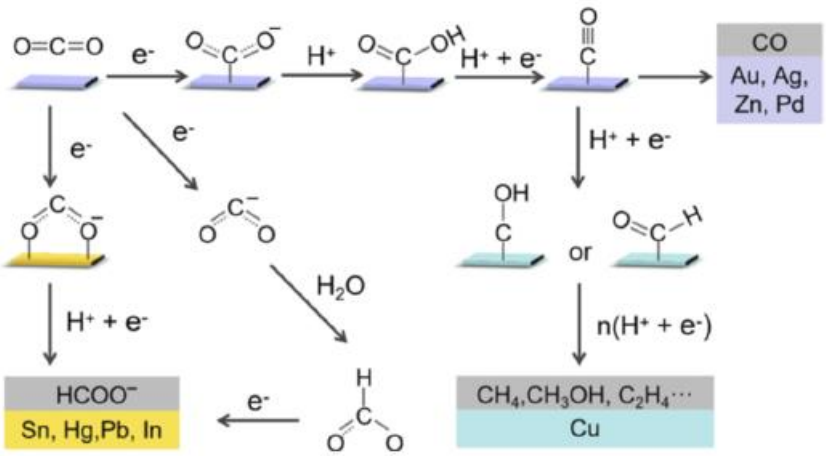

Figure 3 *CO_2 reduction mechanism proposed by [11] Z. Yang, F.E. Oropeza, Copyright 2018 American Chemical Society.*

Carbon monoxide and formic acid, for example, are both formed after a two-electron exchange reaction, the difference in selectivity between these two reactions is based on the type of CO_2 – surface bond. Carbon monoxide formation generally consists of a three-step mechanism, in the first step CO_2 bonds the catalyst surface with the carbon atom, in the second step the hydrogenation reaction on the oxygen atom

occurs, and in the third step the dehydration reaction allows CO to be released from the catalyst surface. Contrary to the CO formation, formic acid needs the oxygen atoms to bind the catalyst so that the hydrogenation reaction can take place first on the free carbon atom and then on one of the oxygen atoms releasing HCOOH.

The production of methane and methanol begins with the same mechanism as the synthesis of CO, when CO is formed on the surface of the catalyst, different hydrogenation reactions allow the release of CH_3OH or CH_4. The only reaction with a different type of bonding is the synthesis of ethylene and ethanol, this class indeed starts with the formation of CO on the surface followed by C – C coupling reactions, crucial for this mechanism is the catalyst's binding energy, in case this is too low the CO will be released too quickly from the surface resulting in the inability for the carbon atoms to couple, on the contrary, if the binding energy is too high the CO will poison the catalyst and the synthesis yield will consequently decrease. The only efficient metal catalyst for C – C coupling by the electro synthesis method discovered nowadays is Copper. It is questionable whether one of these previously described routes is more convenient than the others for the CCU. Even if the answer is still debatable, techno–economics analysis [2] has shown small molecules such as carbon monoxide and formic acid to be more profitable for industrial scale-up due to the lower amount of electrons required for the process (only two electrons for their reduction), the higher selectivity achieved, and the simplicity of controlling and designing the process on an industrial scale.

2. State–of–the–art reactor engineering for CO_2 electrochemical reduction

Electrochemical reduction of CO_2 is a non-spontaneous reaction as such the linear carbon dioxide is the thermodynamically favoured product, thus, to make the reaction possible, it is necessary to supply energy to the system. The conversion of CO_2 is performed in a specific cell called electrolyzer, this configuration is the equivalent of a galvanic cell in which instead of obtaining current from the reaction involved, current is supplied from an external source to push the reaction in the opposite direction of the thermodynamic path.

Electrolyzers, like galvanic cells, are constituted of cathodic and anodic compartments, electrolytes, and selective membranes. One of the simplest and oldest configurations invented is the H-cell, which is a batch cell where the CO_2 availability lies on its

solubility in the electrolyte solution. More advanced electrolyzers, have been developed to have a continuous CO_2 feed, which requires modification in the overall engineering.

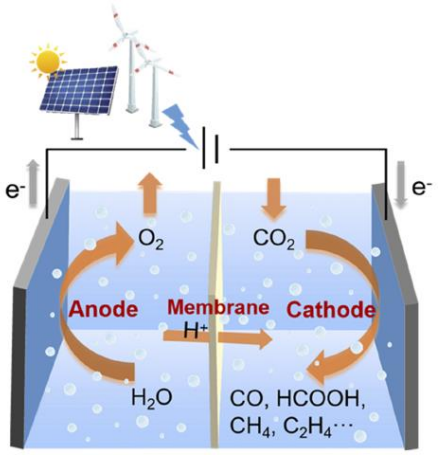

Figure 4 *Schematic representation of electrochemical CO_2 reduction system adapted from Wu et al. 2017, by Z. Yang, F.E Oropeza, and K. H. L. Zang [11], Copyright 2017 Wiley-VHC.*

In those electrolyzers, the CO_2 reduction process involves reactants in three different physical states (CO_2 gas, liquid electrolyte, and solid electrode), thus, a key component is needed to enable this process, and many studies have revealed good results by employing gas diffusion electrodes (GDEs) as one of the most efficient ways to conduct the process by making the interphase contact possible.

The following paragraphs will describe the main components of state-of-the-art engineering available to make CO_2 conversion a feasible process such as the working electrode, the electrolyte and the polymeric membrane.

2.1 Gas diffusion electrode

One of the crucial factors in the electro-reduction of carbon dioxide is the three-phase boundary, i.e. the place where the CO_2 gas flow converges the liquid electrolyte flow at the solid electrode surface, to gain the supplied current and be converted.

To enable the thermodynamics of the reaction, a catalyst is usually adopted to overcome the overall energy barrier of the process, thus, it is fundamental to support the catalyst on the three-phase boundary layer. Many studies [5] have revealed gas diffusion electrodes as one of the best options to enable and achieve high reaction rates.

This new catalyst configuration consists of three-layer components:

- The gas diffusion layer (GDL), is usually a hydrophobic macro-porous fibres carbon layer used to control the gas flow directed to the catalyst, but it also has a structural function as the backbone of the entire GDE.
- The microporous layer (MPL), this component is supported on the GDL and usually consists of a mixture of carbon black particles and hydrophobic materials such as polytetrafluoroethylene (PTFE), its purpose is to diffuse the current density provided at the electrode in the overall surface and prevent the liquid mass transport into the gas flow.
- The catalyst layer (CL), is the top layer supported on the MPL, its purpose consists of making the contact possible between the liquid phase and the gas phase on the catalyst surface, facilitating the reaction process. Many tests [3] have revealed spray coating as one of the best options to support the catalyst on the GDE due to its easy and fast management with high results in terms of selectivity of the final process, considering also its easy and straight upscaling, it is preferred over other fixation techniques such as electrodeposition. The catalyst is usually supported on the MPL in a mixture with an ionomeric fluoropolymer solution (typically Nafion) due to its ability to bind the PTFE contained in the MPL allowing to increase in the electrochemically active surface area, enabling the ionic conductivity to and from the catalyst, and allowing good wettability of the catalyst surface.

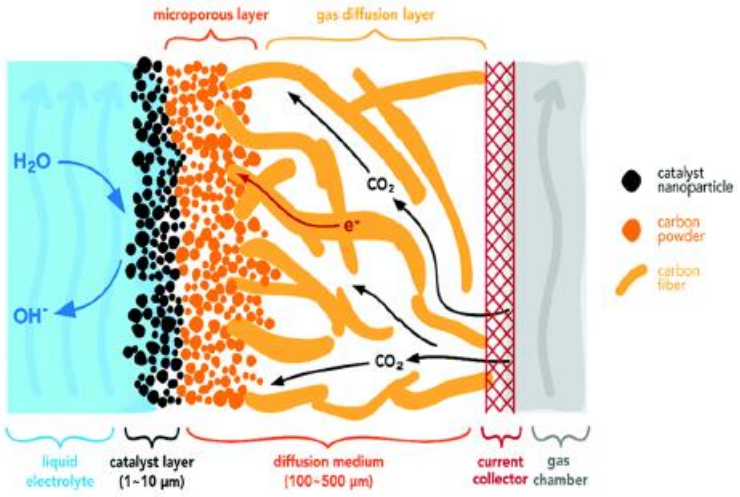

Figure 5 *Schematic of the GDE structure, illustrated by P. Duaarah, D. Haldar, V. Yadav, and M. Purkait [4] by permission of L. C. Weng et al., Chem. Phys. 2018.*

GDEs allow reaching current densities more than an order of magnitude higher than the traditional H-cell configuration used previously, where, only dissolved CO_2 can react at the solid catalyst interface. Due to the low solubility of CO_2, mass transfer will limit the amount of CO_2 that can react, lowering the maximum current density

achievable. Many studies have demonstrated the effect of high current density on mass transport phenomena; indeed, the CO_2 concentration on the catalyst surface in a typical H-cell configuration when a current density above the limiting current density is applied (typically 50-60 mA/cm^2), drops to zero, making mass transport the limiting process. When this phenomenon occurs, there is a shift in selectivity toward the hydrogen evolution reaction due to the constant presence of water on the catalyst surface.

GDEs are an effective solution to better control carbon dioxide mass transport and maintain high CO_2RR selectivity even at current densities around 100-200 mA/cm^2.

2.2 Electrolyte

The main purpose of the electrolyte is to enable ionic conductivity within the system and to allow mass transport to and from the GDE surface. There are several classes of electrolytes based on the reaction involved. In an electrolyzer as in a galvanic cell, the two electrode compartments are divided by the membrane, and two different electrolytes could be employed. Depending on the compartment in which it is used, the electrolyte is called for the anodic and the cathodic compartment is called anolyte and catholyte, respectively. In most of the CO_2 electrolyzer, while the cathodic reaction is the CO_2 reduction, the oxygen evolution reaction (OER) takes place in the anodic compartment.

Oxygen evolution reaction OER

$$2H_2O \rightarrow O_2 + 4e^- + 4H^+ \qquad \Delta E^0 = 1{,}23 \text{ V vs RHE}$$

OER is suitable for this process due to its reaction potential (typically 2.0 V depending on the pH of the solution) affordable for the overall system, its easy development, and low implementation cost, which can be performed in an alkaline solution. Typical anolytes used for this process are potassium hydroxide KOH or potassium hydrogen carbonate $KHCO_3$ both in different concentrations. The use of KOH is often preferred because it reduces the overpotential needed to activate the OER and lowers the ohmic resistance of the system due to its high pH at low concentrations.

The cathodic compartment, like the anodic semi-cell, requires the use of an alkaline catholyte, one of the most widely used is $KHCO_3$.

Potassium hydrogen carbonate is best suited to this role due to several reasons. First, due to the pKa of HCO_3^- it allows performing the CO_2 reduction in alkaline pH around

9 units (when a concentration of 0,5M is employed). Alkaline pH promotes the carbon dioxide reduction instead of the hydrogen evolution reaction (HER), the side-reaction that occurs due to the high proton concentration on the surface electrode at low pH to produce H_2, consequently causing a decrease in selectivity for the target product. Second, $KHCO_3$ is employed because of its pH buffering effect. In a continuous flow reactor configuration such as the catholyte electrolyzers, the electrolyte could be (re)cycled and $KHCO_3$ could prevent an appreciable pH change caused by the CO_2 solubility into the intermediate to form CO_3^{2-}. Although the CO_2 should enter the three-phase boundary layer on the catalyst surface, it is critical to avoid its solubilisation in the liquid phase and subsequent mass transport to the liquid bulk leading to reagent loss and productivity decrease. Furthermore, the cationic species involved in the cathodic compartment must be considered for the catholyte selection. The behaviour of cations in the activity of the reduction process at the WE has been studied and it is now clear that the hydration shell of the cations plays a key role. In particular, it has been shown by S. Ringe, K. Chan, et al. 2019 [12], how different cation sizes influence the reduction mechanism, in fact, the larger the cation the higher the process activity (for example $Cs^+ > Rb^+ > K^+ > Na^+ > Li^+$) due to the lower hydration shell that allows the larger cations to be absorbed on the electrode surface and interact with the reactants, resulting in higher CO_2 reduction activity (Figure 6). In particular, it is commonly believed that due to the smaller hydration shell that allows those species to be better absorbed on the electrode surface, larger cations have a higher concentration on the electrode surface, leading to a decrease in the double layer thickness, making the CO_2 diffusion to the electrode surface faster and the selectivity higher [12]. For these reasons, $KHCO_3$ is considered the best option as a catholyte for the eCO_2R.

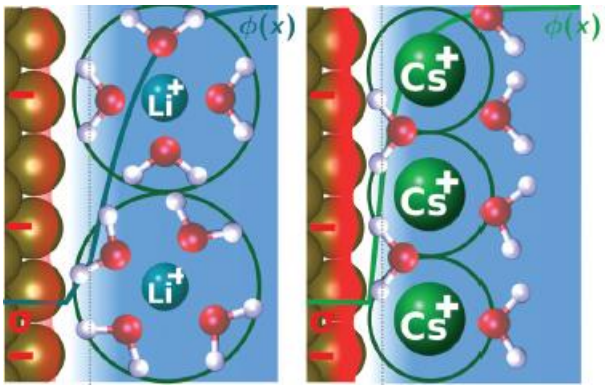

Figure 6 *Schematic illustration by S. Ringe, K. Chan, et al. 2019 [12] of the cation effect on the electrode surface charge and double layer size by solvation of the respective cation species.*

2.3 Polymer electrolyte membrane

In the electrochemical CO_2 reduction (CO_2ER), the electrolyzer is divided into the cathodic and the anodic compartment by a membrane, that allows ionic conductivity and closes the circuit within the cell. Different types of membranes differ in the type of ionic species that can be exchanged, the most commonly used for CO_2ER is typically a cation exchange membrane such as Nafion. This membrane is obtained from a polytetrafluoroethylene backbones structure with perfluoro vinyl ether groups terminated with sulfonate groups.

Due to its polarity, Nafion is a hydrophilic ionomer capable of exchanging protons using the Grotthuss mechanism, in which the sulfonic groups of Nafion can "hop" protons using water as an intermediate receiving the ionic species. The characteristics of Nafion are determined by the humidity grade, the higher the water concentration between the polymer chains the higher the ion conductivity. The thermal stability allows its use up to temperatures around 85-100 °C after which the softening of the polymer begins, and at 190 °C when the glass transition temperature is reached and the polymer will start to melt.

For more extreme conditions, a different polymer, such as poly-benzimidazole (PBI) could be applied. This polymer is obtained by the reaction between the monomers diphenyl isophthalate and 3, 3' diaminobenzidine in a two-step condensation reaction. This polymer uses a different proton exchange mechanism that allows it to avoid the use of water. The mechanism is possible only when the PBI is doped with an acid solution like phosphoric acid. In the doped structure, the phosphoric group assumes a negative charge and can exchange protons using the "hop" method described by the Grotthuss mechanism between phosphoric groups, avoiding the water intermediate. This characteristic enables the polymer to be used up to 100°C at which temperature the water contained in the polymer would otherwise start boiling. The thermal resistance of pure PBI is around 420-430 °C, in this range the glass transition begins and continues up to 500 °C, when thermal degradation of the polymer starts. Excellent performance is obtained between 120°C and 200°C, lower temperatures do not sufficiently activate the polymer. PBI has not been developed enough for use in large-scale applications because of its low activity at low temperatures and high production costs, making it a worse candidate than Nafion for the CO_2ER process.

2.4 Electrolyzers

As previously mentioned, the eCO_2R can be performed in different electrolyzer configurations.

The next few paragraphs will briefly explain all the state-of-the-art reactor designs, with a main focus on the catholyte reactor technology used primarily in this thesis project.

2.4.1 H-Cell reactor

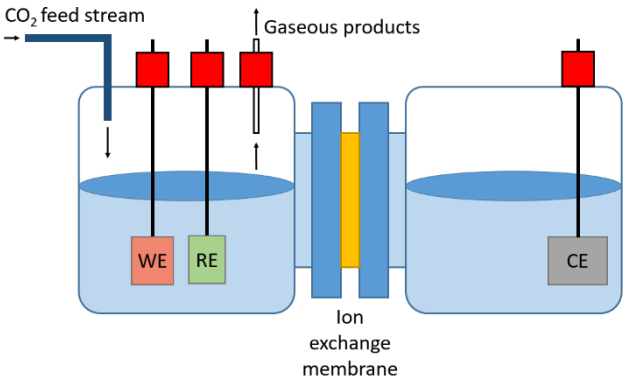

Figure 7 *H-Cell electrolyzer configuration.*

The simplest configuration for the CO_2ER consists of two compartments (anodic and cathodic) separated by a membrane; this configuration is also referred to as the H-cell. The overall system generally consists of three electrodes; the working electrode is placed at the cathodic compartment where the reduction reaction takes place. In the anodic compartment, the counter-reaction usually performed is the oxidation of water to oxygen (OER), although this is not the only option, as will be briefly discussed in the next section. Generally, besides the working and the counter electrodes, a reference electrode, placed in the cathodic section, such as Ag/AgCl, is commonly used to measure the semi-cell potential at the WE. The reference is essential for determining the working potential at which the reaction takes place, but to avoid any alteration as the potential changes, the current is always applied between the CE and the WE, while the potential is read between the RE and WE.

The H-cell configuration unlike the electrolyzer set-ups that will be discussed in the following paragraphs, is a batch cell; indeed, the electrolyte is not (re)circulated and the CO_2 feed is not continuous. The available reagent concentration is therefore limited by the CO_2 solubility in the electrolyte (33 mM at 1 atm and 25°C) and by its diffusion to the electrode surface. These characteristics allow H-cell configurations to be used only at low current density, not exceeding -50 mA cm^{-2}.

The mass transfer from the liquid bulk to the electrode surface, at high current density will not be fast enough to maintain a constant concentration of reactant at the electrode surface, shifting the faradaic efficiency towards the main side reaction such as the hydrogen evolution reaction due to the high concentration of water always present near the electrode.

In conclusion, the H-cell represents an optimal configuration to obtain stable results in a controlled and reproducible environment, but when it comes to high current densities, it is considered a better option to switch to other electrolyzer configurations developed to scale up the CO_2ER to higher current densities, required for large industrial scale.

2.4.2 Catholyte reactor

The catholyte electrolyzer (Figure 8) is one of the most extensively studied reactors, like the H-cell configuration, it consists of two compartments, in which the reduction reaction and the counter oxidation take place. In the cathodic compartment, the electro-catalytic CO_2 reduction takes place on the working electrode and vice versa at the anodic compartment, an oxidation reaction, commonly OER is performed on the counter electrode.

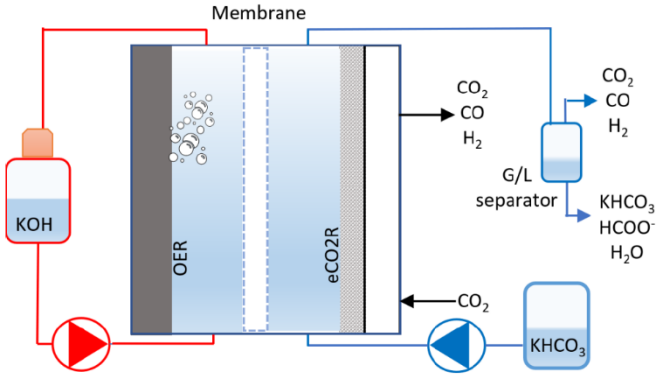

Figure 8 *Catholyte electrolyzer configuration, Source: [3] B. De Mot, 2022.*

Contrary to the H-cell configuration, the catholyte reactor allows to perform analysis in continuous flow, where the CO_2 is continuously fed to a gas diffusion electrode (GDE). On the GDE surface, the three-phase boundary layer composed by the catalyst supported on the electrode surface, the carbon dioxide, and the catholyte enables the reaction.

For these reasons, the GDE as mentioned above is a key component of the overall configuration, especially when dealing with particular temperature and pressure conditions.

The general set-up of the catholyte reactor is usually composed of 7 different parts (Figure 9):

A. Metal plates & plastic insulators: used to assemble all the reactors components;
B. Copper current collector;
C. Graphite plate: etched to obtain channels in which the gas flow can reach the three-phase boundary layer on the GDE;
D. Gaskets;
E. Gas diffusion electrode (WE) & Nafion membrane;
F. Graphite plate: etched to obtain channels where the liquid can flow and reach the counter electrode.
G. Counter electrode (CE) usually Nickel foam.

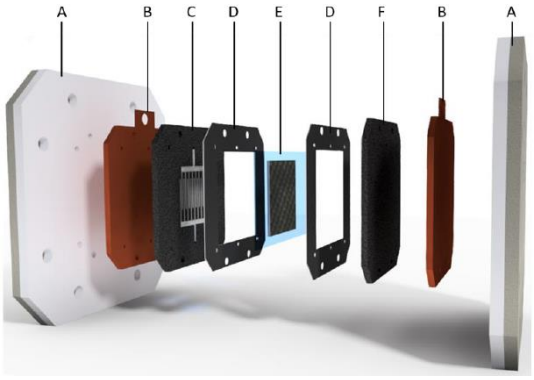

Figure 9 *Catholyte reactor's main components.*

The working and the counter compartment are separated by a Nafion membrane to maintain stable ion conductivity inside the reactor, where two different electrolytes are employed.

The CO_2ER performed at the working electrode requires a catholyte made usually by $KHCO_3$ (usually 0,5M), the counter compartment, on the other hand, requires a high pH to promote the oxidations reaction, which is why the anolyte usually adopted is KOH (usually 2M), which allows a pH around 14, at which the activity of oxygen evolution reaction increase. OER, as mentioned above is the main reaction performed at the counter electrode due to its easy execution, but other reactions can be coupled to obtain more valuable products and make the overall process more economically feasible for the large-scale industry. One example would be the electrochemical oxidation of alkanes to olefins. Achieving this goal may require higher temperatures and pressures, the consequences of these conditions on the overall electrolyzer configuration will be described later in this paper.

To conclude the description of the catholyte set-up, it is essential to also provide the difference between the two main configurations on which this reactor is based. The main difference lies in the way the CO_2 flow reaches the working electrode, also leading to different challenges in its execution.

The catholyte electrolyzer, in general, can be differentiated into flow-by reactor and flow-through reactor (Figure 10).

Whereas in a flow-by system, the graphite plate of the cathodic compartment has continuous channels so that only a portion of the total carbon dioxide flow will reach the three-phase boundary layer on the GDE, in the flow-through system, the channels are split, forcing the CO_2 to flow through the GDE. Generally, flow-by configurations are preferred since the flow-through system often leads to problems such as salt deposition and bubble formation on the catalyst surface, resulting in a decrease in efficiency due to a drop in the electrochemically surface area and an increase in ohmic resistance.

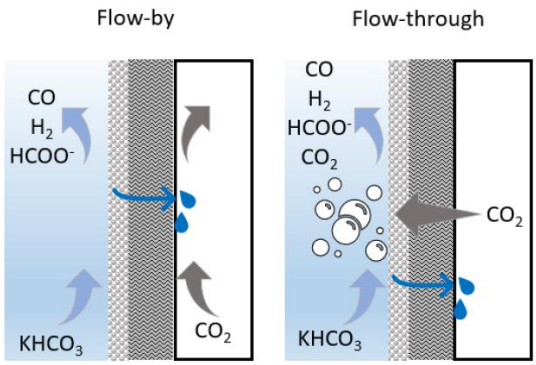

Figure 10 *Catholyte flow-by(left) and flow-through (right) configurations, Source: [3], B. De Mot, 2022.*

The catholyte system has been developed toward several configurations after many studies that tried to solve problems to achieve a feasible configuration for the scale-up of the overall process.

The following paragraphs will describe the state-of-the-art electrolyzer configurations, that have emerged from the studies conducted on the previous catholyte reactor.

2.4.3 Zero Gap Reactor

The zero gap electrolyzer (Figure 11) is obtained by removing the catholyte compartment from a catholyte reactor, resulting in a GDE that is pressed against the membrane.

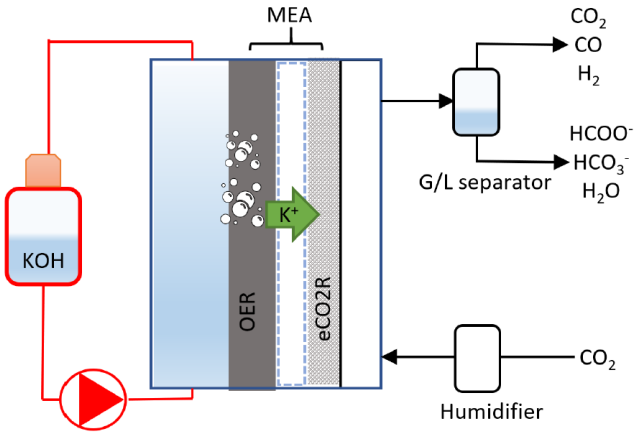

Figure 11 *Zero Gap electrolyzer configuration, Source [3], B. De Mot, 2022.*

Removing the catholyte compartment reduces the overall cell potential because of a lower ohmic resistance of the reactor, thus increasing the energy efficiency. Furthermore, it results in a lower chemical consumption of the overall process, as no catholyte is used. In this setup the CO_2 is fed directly to the GDE surface located near the membrane; the main problem associated with this configuration is the easy salt deposition that takes place due to a large portion of CO_2 flowing through the GDE and reacting with hydroxyl groups (largely present as side products of the water splitting at the cathode to provide the protons needed for the CO_2 to be converted to other chemicals) forming carbonic acid. Avoiding salt deposition is fundamental to maintaining high selectivity and high activity of the electrochemical surface area of the GDE, so to solve the problem usually CO_2 is fed in a mixture with water. The water flow rate can have a substantial impact on the efficiency of the process as the product concentration decreases at a high water flow rate and the diffusion of CO_2 to the GDE is hindered by the water supply. In contrast, a low water flow rate does not prevent the reaction between the carbon dioxide and hydroxyl groups, which can easily lead to carbonic acid formation and consequently induce salt deposition.

In a zero-gap configuration, the membrane plays a crucial role. The most common configuration uses a cation exchange membrane (CEM) that allows only cations to reach the cathode, anionic exchange membranes (AEM) are also employable but due to the hydroxyl group movement toward the CO_2 flow, they achieve higher salt deposition rates. Alternatively, many studies also involve the use of bipolar exchange membranes where the water is split into cations and anions at the center compartment of the membrane, and then the cations move toward the cathode while the anions

move toward the anode. Bipolar membranes are not yet suitable for this kind of configuration due to their low stability at high current density and high ohmic resistance. Overall the performance of the zero gap configuration is still inferior to that of the catholyte configuration in terms of current densities achieved [3]. This behaviour is mainly caused by the inability to control the pH on the surface of the GDE, which results in a high loss of CO_2 by a cross-over reaction with hydroxyl groups.

2.4.4 Three-Compartment Reactor

The three-compartment electrolyzer (Figure 12) consists of three different compartments separated by two different membranes, a CEM pressed against the counter electrode (anode) and an AEM pressed against the working electrode (cathode), a solid electrolyte is usually placed between the two membranes, which allows high ionic conductivity without the need for a liquid electrolyte.

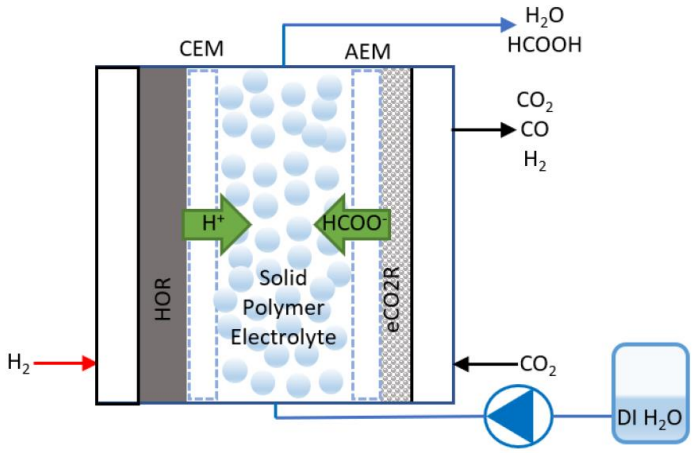

Figure 12 *Three-compartment electrolyzer configuration, Source [3], B. De Mot, 2022.*

The thickness of the latter component determines the overall cell voltage due to the ohmic resistance it provides. The overall process consists of converting the CO_2 on the GDE surface and then diffusion of the anions produced through the AEM and into the solid electrolyte. The anions produced meet the cations produced at the anode by Hydrogen oxydation and evolution reaction (HOR), after which are diffused through the CEM to form the final product. A clear example is CO_2 conversion to formic acid.

At the cathode, formate is produced, which can diffuse through the AEM into the solid electrolyte until it faces the protons produced by the anode and diffused through the CEM to give the final formic acid.

The process has very high productivity since there is no liquid electrolyte, resulting in a very high concentration of the formic acid produced. This condition can also be a disadvantage since the high formic acid concentration could induce a cross-over

reaction at the cathode. One method used to maintain high selectivity is increasing the thickness of the CEM to stop the crossing of the membrane and keep the faradaic efficiency constant.

In the case of formate, water is supplied at the middle compartment to provide a source of proton allowing the formic acid formation, then the resulting product will be solubilized into the outgoing water stream ready to be separated.

2.5 Reactor stability

Several factors can affect the CO_2ER process, such as pressure, temperature, and different current densities adopted. Each condition can affect the reactor configuration differently.

2.5.1 Effect of temperature

One of the advantages of electrochemical processes is the use of current to overcome the thermodynamic barrier and promote either the kinetic of a reaction without resorting to extreme conditions of temperature and pressure. Nonetheless, as mentioned earlier, the performance of an electrolyzer in terms of productivity and profit can be increased when combined with different reactions to obtain valuable products such as the oxidation of paraffins to olefines. To perform such reactions, higher temperature conditions cannot be avoided.

In those cases, many studies are still underway to better understand the effects of temperature on the electrolyzer configuration.

The main components affected by the increase in temperature in a common electrolyzer are the electrolyte, the membrane, and the GDE.

When a high temperature is applied, the ionic conductivity of the electrolyte increase because the kinetic energy of the ionic species rises with the temperature, therefore a decrease in activation and diffusion over potential is also observed. This effect has to be considered in parallel with the change in the solubility of CO_2, the change in surface tension, and the change in the value of the diffusion coefficient. The overall behaviour is indeed the result of the balance of all these consequences [6]. As the temperature rise, the solubility of CO_2 in the liquid phase of the three-phase boundary layer decreases due to the change in Henry's constant in accordance with the Van't Hoff equation.

$$\frac{d\ lnH}{d\ T^{-1}} = \frac{-\Delta_{sol}H}{R}$$ *Van't Hoff equation*

H: Henry's constant

T: temperature

R: gas constant

$\Delta_{sol}H$: enthalpy of dissolution

This event leads to a lack of CO_2 on the catalyst surface, which consequently leads to a shift in faradaic efficiency towards HER. On the contrary, as the temperature increase, the diffusivity of species within the liquid phase increase due to an increase in the diffusion coefficient. In accordance with Fick's law, the diffusion and back diffusion from and to the bulk of the liquid phase will be faster for both CO_2 and the target product, maintaining a constant concentration of reactant through the diffusion layer and onto the catalyst surface, avoiding the side HER.

$$J = -D\ \frac{\partial C}{\partial x}$$ *Fick's first law*

$$D = D_0\ exp\left(\frac{-E_a}{RT}\right)$$ *Dependency with temperature*

J: mass flow

D: diffusion coefficient

D_0: maximal diffusion coefficient

E_a: activation energy

R: gas constant

T: temperature

C: concentration

X: position

Considering both behaviours, an increase in temperature leads to a maximum point at which the effects balance. It has recently been discussed in many studies [6] that 50 °C might be the optimum temperature to obtain the best performance in a common electrolyzer for the CO_2ER, although the results are still questionable as further studies need to be performed. The effect of temperature on the GDE is mainly the reduction of surface tension of the electrolyte, which allows the liquid phase to more effectively "wet" the catalyst surface on the GDE, decreasing the contact angle between the liquid-solid interphase and leading to flooding of the electrolyte toward the gas phase.

Flooding of the electrolyte across the GDE is critical, as it is considered one of the main causes of activity declines [1], as the liquid flow blocks the porosity of the catalyst, reducing the electrochemically active surface area and leading to salt deposition on the catalyst.

Furthermore, in a common electrolyzer such as the catholyte one, the Nafion membrane is used to divide the compartments of the cell, which will also be influenced by changes in temperature. Nafion is particularly sensitive to temperature change because its conductivity is based on the Grotthuss mechanism and uses water as an intermediate for the exchange of ionic species. Increasing temperature first decreases the water content of Nafion, resulting in polymer stiffening, swelling, and loss of conductivity; finally, carbon–sulfur bonds also break, resulting in fine cracks on the polymer. For these reasons, Nafion membranes are not recommended for usage over 80-90°C.

2.5.2 Effect of pressure

In a catholyte reactor, two different pressures can be identified on the sides of the GDE, attributed to the gas and liquid phase, respectively.

Three scenarios have been studied:

- Positive net pressure
- Negative net pressure
- Neutral net pressure

In the first case, the liquid pressure is higher than the gas one, this condition leads to flooding of the electrolyte through the GDE, as mentioned earlier in the case of high temperatures, the flooding causes a decrease in the catalyst activity.

In the second case, the gas flow is circulated with a pressure higher than that of the electrolyte side of the GDE. This condition stops the flooding of the electrolyte but can also cause structural overstressing of the electrode. In addition, it results in the loss of CO_2 in the electrolyte due to the crossover of the GDE, subsequent solubilization in the liquid, and finally a drop in productivity.

The last case proved to be the best performing, with no particular liquid flooding or gas crossover of the GDE.

2.5.3 Effect of high current density

To explain all the possible causes of the destabilization of the electrolyzer configuration, it is also necessary to mention the current supply.

High current density, enables to perform thermodynamically more unfavoured reactions, leading to the overcoming of the energy barrier between the stable reagent and the less stable products. It also increases the kinetic of the reaction and helps to achieve the over-potential needed to overcome all the resistances in the system. In terms of GDE, high current density leads to an increase in the critical phenomenon called "electrowetting". Electrowetting is the change of contact angle between a solid surface and a liquid due to a different potential between the two phases. This event can be observed as the loss of hydrophobicity of the PTFE layer on the GDE caused by its electrification at high current density. The higher the current delivered, the greater the electrowetting and ultimately the flooding through the GDE with salt deposition on the porosity of the latter.

3. Electrocatalysis of CO_2 to formic acid

It has been mentioned previously in this work, how small molecules such as carbon monoxide and formic acid are the most suitable for the CO_2ER process, as their costs of production and process designs are more feasible for a future scale-up. In the following paragraphs, the production of formic acid as a precious building block and its role in the CCU process will be discussed.

3.1 Traditional production of formic acid

Formic acid is the simplest form among carboxylic acids with the chemical formula HCOOH; it is a colourless liquid with a distinct smell. It is one of the most important building blocks in industrial chemistry, and its global market reached 710 thousand tons in 2021 according to the ChemAnalyst report. Its applications range from the preservative sector, due to its antibacterial properties, where it is used as an animal feed additive, and as a fungicide to other sectors such as fermentation, soldering, fuel cells, textile, leathers, and cleaning. Currently, China and Europe are major producers of formic acid, and BASF holds the highest capacity in this market.

In the late 1900s, formic acid used to be produced and sold as a by-product of the process of hydrocarbon oxidation to acetic acid. In this process, a mixture of hydrocarbons is used to obtain acetic acid and several by-products, most notably

HCOOH. The whole process is catalyzed by cobalt acetate or chromium acetate and is carried out at temperature and pressure conditions of 150 – 230 °C and 50 – 60 bar, respectively.

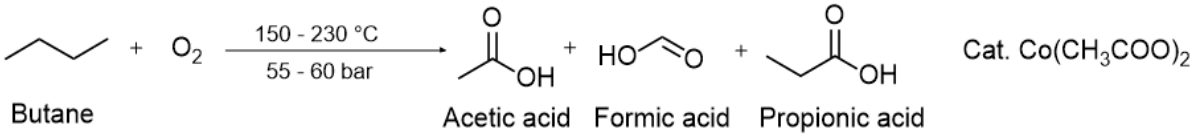

Figure 13 *Hydrocarbon oxidation to acetic acid.*

In recent years, the production of acetic acid has evolved to an environmentally friendly route through the carbonylation of methanol using the “Cativa” process, avoiding obtaining cheap formic acid as a by-product. Formic acid production has consequently taken other directions, and many other processes have been considered for the global production. One of the main routes currently used is the hydrolysis of methyl formate, which covers 90% of the installed capacity of formic acid production.

The synthesis consists of a two steps mechanism of carbonylation of methanol to methyl formate and subsequent hydrolysis to produce formic acid and methanol, which can be reused in the first step. The reaction is performed in an alkaline intermediate using a sodium methoxide or potassium methoxide catalyst.

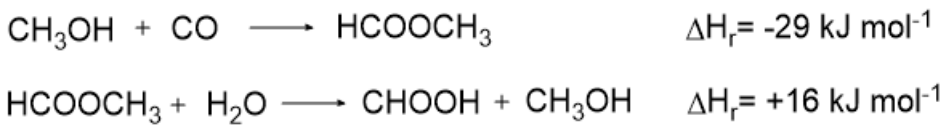

Figure 14 *Carbonylation and hydrolysis reaction steps.*

The carbonylation step is typically conducted at 80°C, 4,5 MPa, and 2,5 wt% of sodium methoxide, yielding a conversion of 30% for methanol and about 95% for carbon monoxide. One of the problems with the synthesis is the production of formate salt caused by the side reaction of the catalyst with methyl formate and water. For this reason, it is important to make sure to have negligible humidity of the reagent feed and a stoichiometric amount of catalyst.

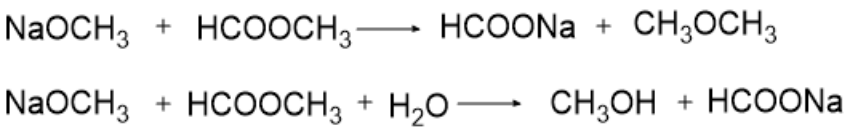

Figure 15 *Side deactivation reactions of the catalyst.*

The industrial process performed by BASF to produce formic acid is shown in Fig. 16.

In this flow sheet, the first synthesis step is performed in the methyl formate reactor, while the second step is performed in the hydrolysis reactor. Between these two phases, the methyl formate column allows the separation of the methyl formate produced by the first reaction step from the solution of methanol and the dissolved catalyst. After the second step, a distillation process is performed to recycle the methyl formate and methanol in the hydrolysis reactor and to remove the water and formic acid solution from the bottom. This is followed by a liquid-liquid extraction with secondary amide within the dehydration column before finally being distilled from the last water content to obtain pure formic acid in 90-98 wt% in the pure acid column.

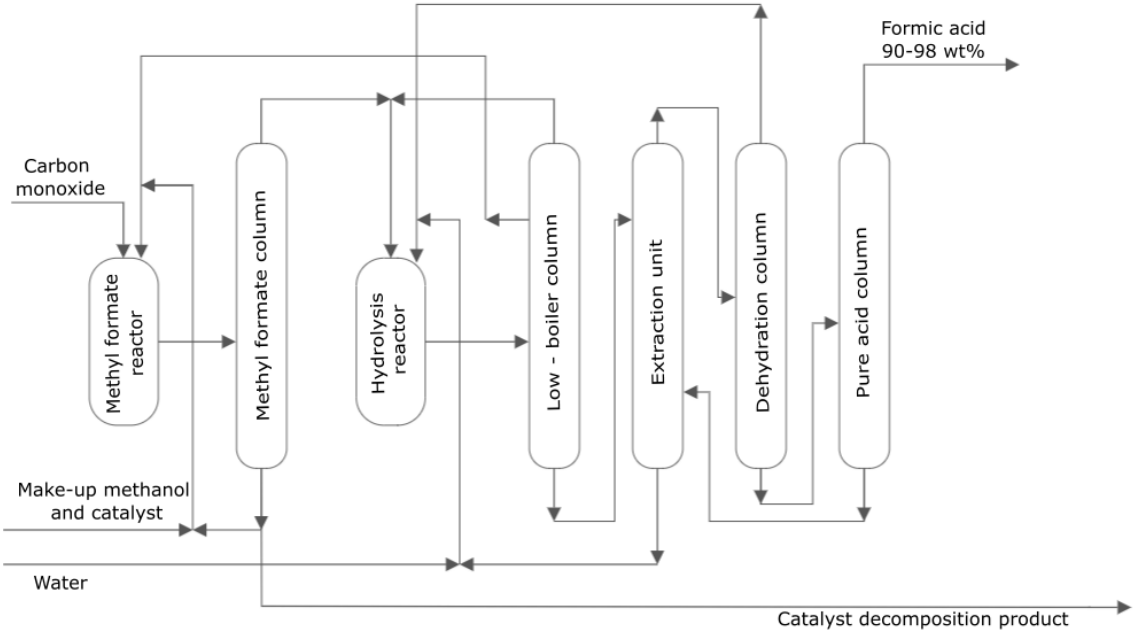

Figure 16 *Formic acid industrial BASF's process.*

3.2 State-of-the-art production of formic acid by carbon capture and utilization

Formic acid production, in addition to the mere goal of satisfying the global market for this product, could aspire to improve global warming mitigation, using raw materials such as CO_2.

One of the most environmentally friendly prospects in this regard is the production of formic acid from CO_2 by electrochemical reduction. This pathway, to be as ecological as possible, requires green electricity and CCU treatment of CO_2 emitted as flue gas. As early mentioned, the electrochemical reduction process is an intriguing technique with several advantages, such as controllable reaction parameters (temperature, pressure, electrolysis potential), great scaling-up potential, and flexible with the source of electrical energy that use to drive the process [4].

To achieve this economically-feasible process, techno-economic analysis has shown that is critical to operate CO_2ER electrolyzers at current densities over 100 mA cm^2 for industrial applications, to ensure that the capital cost of the electrolyzer is in an acceptable contribution range to the total product cost [10]. Therefore, an optimum current density value of around 200 mA cm^{-2} is expected for industrial applications, with a catalyst durability of 1000 hours for CO_2 to HCOOH conversion processes.

In Europe, according to Eurostat statistics based on electricity production, consumption, and market overview published in 2023, the total amount of net electricity in the European Union in 2021 was 2785 TWh. The total electricity supply can be differentiated into different sources, among which only 33% derives from renewable sources such as solar energy (5,8%), wind energy (13.7%), geothermal energy (0.2%), and hydropower (13,3%). The rest of the total current production is still based on fossil fuels sources (41,9%), nuclear power (25%), and others (0,1%).

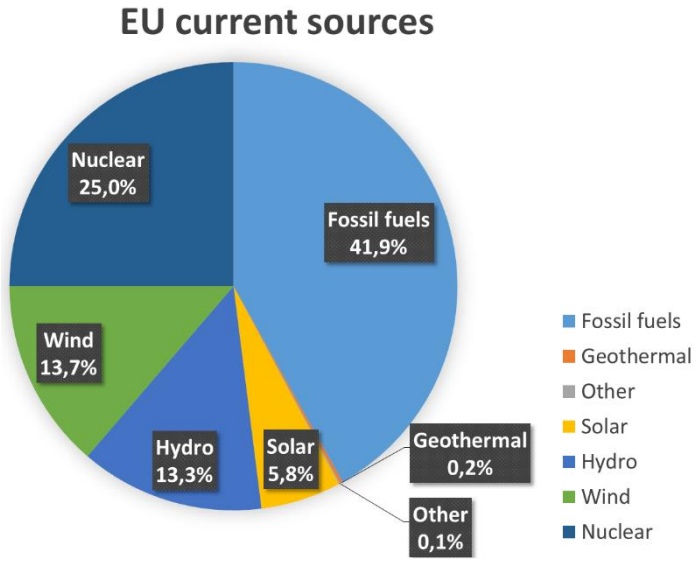

Chart 1 *EU current supply, Source: Eurostat 2021.*

Considering the total amount of formic acid produced by Europe to be around 350 kilo tons, and assuming the ability to perform the CO_2 conversion to formic acid at 200 mA cm^{-2} with a total cell voltage of 3,52 V in a three-cell compartment as H. Yang and J. Kaczur pointed out [10], the total amount of current required\ to satisfy the HCOOH European production would be 0,5896 TWh, which is the 0.064% of the total green current produced at the moment by the European Union.

In the carbon dioxide process to formic acid at low temperatures several limitations are still challenging the scale-up process, such as the catalyst stability and subsequent selectivity to the target product.

To tackle this challenge many studies evolved on different electrolyzer configurations, electrolytes, and catalysts to better understand and optimize the performance of the large-scale process.

The latter is particularly critical because, as mentioned earlier, the thermodynamic barrier for the formation of HCOOH from CO_2 requires a large amount of energy to be overcome, resulting in a large cell potential and the need for high current delivery. Furthermore, since the HER and CO_2ER occur in a similar potential range (-0,83 V and -1,078 V vs RHE), it is essential to have high catalyst selectivity for the target product. This work will mainly focus on the activity and characteristics of a novel series of catalysts used for this process, thus an overall explanation of the catalytic mechanism will follow to allow the reader to better understand the critical role of electrocatalysts in this conversion route.

3.3 Electrocatalysts to enable the CO_2 reduction

CO_2 is a highly stable linear molecule, characterized by bond length and energy of 116 pm and 803 kJ mol^{-1}, respectively. CO_2 reduction tends to be endergonic when the O/C ratio of a product is smaller than 2. The thermodynamic stability and kinetics of CO_2 make its reduction challenging, although in aqueous solutions the conversion to HCOOH is considered spontaneous with ΔG^0= -4 kJ mol^{-1} and ΔH^0= -427 kJ mol^{-1}.

The overall reduction process requires 2 electrons for each molecule, in which the carbon oxidation state changes from +4 to +2 (Table 1, No. 3)

Reduction reaction to formic acid

$$CO_2 + 2H^+ + 2e^- \rightarrow HCOOH \qquad \Delta E^0 = -1{,}078 \text{ V Vs RHE}$$

The most energy-consuming step of the process is the formation after acceptance of 1 electron of the radical anion $CO^{\bullet-}$ (Table 1, No. 1). Once the unstable intermediate is generated the reaction can lead to different products based on the type of bonding that will follow in the second electron gaining.

Electrocatalysts allow to lower the redox potential requested to form the radical anion $CO^{\bullet-}$ (-1,9 V vs Normal hydrogen electrode NHE [4]), by forming a chemical bond with the catalyst surface that stabilize the intermediate.

Therefore, the chemical adsorption of CO_2 onto the chemical active sites of the electrocatalyst is crucial to activating the process and it is consequently one of the main parameters to be optimized to improve catalyst performance.

3.4 p-block metal electrocatalysts

The most widely used catalysts for the process, are the p-block metals, among which tin and bismuth have mainly been studied for HCOOH production and showed faradaic efficiency toward formic acid greater than 90% in CO_2-saturated aqueous solutions according to Z. Yang et al. [11].

p-block metals are of particular interest due to their binding energy with the adsorbate, in this case, CO_2. Having their d-bands completely filled and with relatively low energy below the Fermi level, their chemical adsorption with an adsorbate produces a bonding band and an antibonding band, whose energies lie at the equilibrium point between the d-bands and the valence orbitals of the adsorbate.

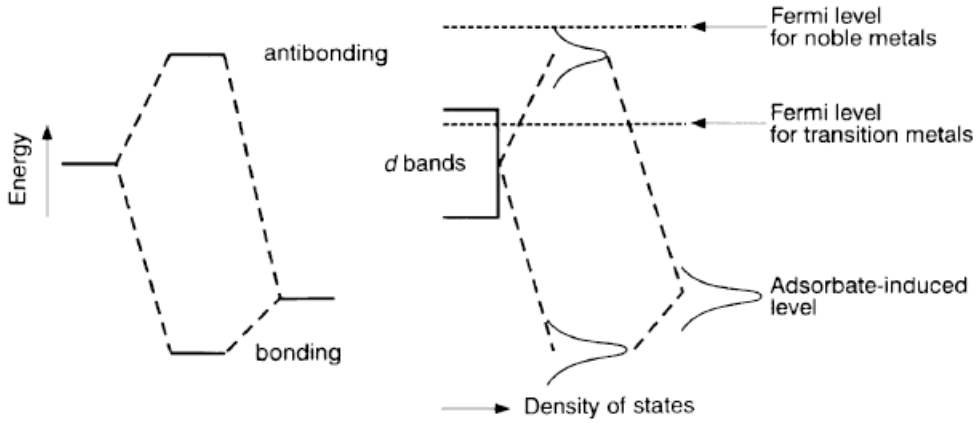

Figure 17 *Electronic states distribution over energy and densities, Source: [gold paper] B. Hammer, J. K. Norskov.*

The p-block metals allow to obtain an antibonding band that lies in energy levels not extremely below the Fermi level and neither above, allowing binding energies with the adsorbate that are not too high, causing surface poisoning of the catalyst and neither too low, leading to avoiding the surface interactions with the catalysts [4].

The suggested mechanism for the reaction that leads to formic acid is composed by the following steps:

- The CO_2 stream diffuses across the GDE to the catalyst layer, where it dissolves into the three-phase boundary layer;
- Once the CO_2 is dissolved in the electrolytes on the catalyst surface, it can start to diffuse from the liquid bulk through the double layer, where it finally gets in contact with the metal surface.
- Two types of interaction take place on the catalyst, first, the physical adsorption allows to obtain a stabilized energy band caused by the interaction between the s band of the metal and the valence orbitals of the adsorbate, then the chemical

adsorption can take place forming the previously mentioned bonding and antibonding bands. The CO_2 can bind onto the catalyst surface in two main pathways, leading to different products as mentioned earlier in this work. In the case of bismuth- or tin-based electrocatalyst, CO_2 approaches the catalyst surface via oxygen atoms, indeed the Bi – O and Sn – O bonds have stronger stability than the Bi – C and Sn – C bonds according to Z. Yang et al. [11], leading to the formation of formate *OOCH instead of carboxylic group *COOH.

- Once the adsorbate is chemically bonded to the catalyst surface, electron transfer can take place. The first electron transfer yields the unstable radical anion $*CO_2^{\bullet-}$, and the subsequent electron leads to obtaining $*CO_2^-$ still adsorbed on the surface. The water contained in the electrolyte enables the proton transfer to the carbon atom forming *OOCH.
- Once *OOCH is formed on the catalyst surface, the second electron transferred to the antibonding band, destabilizes the metal-adsorbate interaction and breaks the chemical bond. The electrolyte will then supply the proton to bind the oxygen atom forming HCOOH, which is now ready to back diffuse to the liquid bulk.

Tin electrocatalyst

Sn–based materials have attracted great interest in recent years due to their high activity and selectivity towards formic acid, their low toxicity, and their abundance in the Earth's crust, which makes them great candidates for the CO_2ER on large-scale processes.

Metallic tin is well known for its tendency to re-oxidize to SnO or SnO_2, however, for its applications in CO_2 reduction, the applied potential to reduce carbon dioxide is more negative than the reduction potential to Sn^0, therefore, during its applications into the formic acid production it is expected to participate in the metallic form from a thermodynamic point of view.

Although, considering the reduction kinetic of SnO and SnO_2 to Sn^0, it is expected either to have metastable oxide species persistent on the electrode surface during the cathodic process. Even if is still not clear whether the CO_2 reduction happens on the SnO_x sites or the Sn^0 sites, the presence of SnO_x may provide an easier pathway to stabilize the intermediate $CO_2^{\bullet-}$ according to Z. Yang et al. [11].

Furthermore, ATR-IR analysis showed that CO_2 can interact with tin, producing stable $Sn(CO_3)_2$ tin carbonates species on the surface, which will after the reduction process liberate HCOOH and get to the previous structural conformation.

One of the disadvantages of using tin is the instability of structure changes at high current densities or temperatures for long-term analysis. To enhance structural stability, since the use of bismuth has already been confirmed to outperform tin, researchers have developed new synthetic routes to obtain tin-based material covered by a thin shell of carbon. The carbon shell, covering the catalysts particles, physically inhibits agglomeration and further oxidation, restoring the selectivity drop associated with the structural changes.

In conclusion, Sn-based electrocatalysts have been studied extremely since the pioneering works made in 1994 by Hori et al. [19], and have shown great performances in the formic acid process in terms of selectivity, activity, and stability at room temperature, providing FE greater than 90% to HCOOH.

Bismuth electrocatalysts

Bi-based materials have not received as much attention as Sn-based materials, even though, more recently, Bi electrocatalysts have shown great performance in the reduction of CO_2 to formic acid, comparable to tin- and indium-based materials.

Generally, Bi materials have a lower HCOOH formation overpotential and higher faradaic efficiency than the Sn-based ones, and are considered the most promising electrocatalysts for industrial applications [11].

Recent studies showed, as with tin, that the particle size, defects, and other physicochemical properties of bismuth play a fundamental role in catalytic performances.

Contrary to previous statements for tin catalysts, the debate on which structural phase performs better among BiO_x and Bi^0 species is still open. Many studies have revealed the presence of unchanged BiO_x species during the reduction process by ATR – IR analysis, therefore, Bi electrodes have been classified as oxide-independent electrocatalysts. On the other hand, many reports have explained the importance of Bi – O interactions with the adsorbate, as the hybridized orbitals obtained from the 6p of bismuth and the 2p of oxygen can promote the electron donation to acid species as CO_2 enabling its adsorption on the catalyst surface. Furthermore, as with tin-based materials, the introduction of defects on the catalyst surface appears to improve the

stabilization of intermediates on the catalyst surface, due to a higher electronic density available in the defects sites, caused by a decrease in the coordination of the metal.
In addition, one ultimate type of species was found during the catalytic CO_2 reduction on the catalyst surface, such as Bismuth carbonates species $Bi_2O_2(CO_3)$. The proposed mechanism for the formation of these species is based on several reactions:

- Metallic bismuth on the surface can be oxidized by the atmosphere, producing Bi^{3+}, which is the most stable oxidation state under normal conditions of temperature and pressure.

$$2Bi^0 + \frac{3}{2}O_2 \rightarrow Bi_2O_3$$

- In the CO_2 reduction process to HCOOH, water works as a proton source, leading to an increasing local concentration of hydroxyl species near the catalyst surface.
- The hydroxyl species lead to the formation of bismuth hydroxide, which is unstable and can ultimately lead to bismuth carbonate.

$$Bi^{3+} + 3OH^- \rightleftharpoons Bi(OH)_3$$

$$2Bi(OH)_3 + CO_2 \rightleftharpoons Bi_2O_2CO_3 + 3H_2O$$

Which species is responsible for the good performance of bismuth-based materials is still unclear, and more research needs to be performed before the correct behaviour can be defined, nevertheless, bismuth is considered one of the most promising catalysts for the industrial-scale CO_2 electro-reduction, due to its high activity, selectivity, low cost, and good performance at high current density and high temperatures, suggesting a better stability of the catalyst structure than tin-based materials.

3.5 Hydrothermal synthesis

Hydrothermal synthesis is one of the most popular methods to produce nanoparticle catalysts. This route uses high pressure and temperature to achieve the thermodynamic conditions where the crystalline growth of the catalyst is initiated through equilibrium between the solubilization and re-precipitation reaction of a low solubility material. Using different couples of pressure and temperature values, it is possible to modify the size and morphology of crystalline particles according to the vapour tension of the adopted precursor. Many structures have been obtained using this approach, such as nanoparticles, nanorods, nanotubes, hallow nanosphere etc. as Gan et al. reported in their work [20]. The technique is easy to perform and has many

advantages such as an easy management of variables to control the morphology of the product, minimal loss of material used for the synthesis, and low amount of time employed. The thermodynamic conditions are usually reached using a Teflon-lined stainless steel autoclave, in which the precursor is placed. High pressure is self-induced by raising the temperature of the autoclave in an oven, at which point the precursor's vapour tension will increase.

Chapter 2

Goals of the project

The second chapter of this dissertation aims to provide the scope and strategy adopted in this project to better interpret the results that will be provided later on.

1. Goals

As mentioned in the first chapter, CO_2 electroreduction can be performed at higher temperatures than room temperature, to facilitate overcoming the thermodynamic barrier of coupled oxidation reactions such as the oxidation of paraffins to olefins.
In this project we aim to study the CO_2 electroreduction in a catholyte flow-by electrolyzer at 85 °C, using a new series of bismuth nanoparticles catalysts, which are claimed to be more stable at higher temperature and current densities than the respective tin-based material.
In order to accomplish this main goal, many studies and adaptations, need to be developed to both the reactor set-up and the catalyst series due to the required temperature change.
The overall project can be divided into four steps:

1. Synthesis of the new catalyst series;
2. Optimization of the reactor set-up using a reference catalyst;
3. Characterization of the catalysts obtained;
4. Performance tests of the new series in the optimized reactor configuration.

The implementation of these steps will provide not only a deep overview on the effects of temperature in the CO_2ER process, but also an alternative class of catalysts to the classic Bi- and Sn-based materials already studied at room temperature.

1.1 Synthesis of the new series of Bi-based catalysts

In order to achieve more stable catalysts after long-term reduction processes and at high temperature and current density, several research teams developed tin-based catalysts with a carbon shell, to decrease the sintering of the nanoparticles. The same concept has been developed in this work using bismuth-based materials (already known for their improved structural stability), changing the starting precursor from the previous synthetic routes created for tin-based catalysts.

1.2 Optimization of the reactor configuration

One of the most encountered problems working on a catholyte reactor, is the flooding of the catholyte through the GDE, and at higher temperature this problem becomes even more important. To reduce this phenomenon one of the variables that can be modified is the gas flow pressure, which can balance the flooding of the liquid.
In order to optimize this criteria:

1. A back pressure valve is applied to control the overall pressure inside the cathode compartment.
2. Each valve set point has been controlled in terms of gas and liquid dynamic pressure using a digital pressure indicator.
3. Several valve set points have been studied in terms of FE using a reference catalyst for CO_2 conversion to formic acid.
4. The best back pressure allowing the higher selectivity, was used in the following steps of performance testing.

1.3 Characterization of the new series of catalysts

To determine the activity and selectivity towards the CO_2 reduction of the newly synthesized catalysts, several studies have been performed.

Starting with physical characterization, the specific surface area, porosity distribution, micro-structure, and crystallinity have been studied using Nitrogen adsorption measurements, scanning electronic microscopy (SEM), and X-ray diffraction (XRD) analyses, respectively. This is followed by chemical activity characterization using techniques such as cyclic voltammetry, linear sweep voltammetry, and electrochemical surface area determination. Ultimately the chemical distribution of every catalyst in terms of bismuth and carbon percentage has been observed using thermogravimetric analysis (TGA) and inductively coupled plasma (ICP) determination.

1.4 Performance tests of the new series of catalysts

The catalysts have been studied in three different levels of analysis, varying from the length of the experiments to the applied current densities. All tests have been conducted at 85°C using the optimized reactor configuration developed during the second step of this project. The catalysts performances have been compared based on their selectivity and cell potential, used as an indication of their stability after being submitted to thermal and electric stress.

Chapter 3
Experimental methodology

This chapter will present the experimental methodology used to develop and characterize a novel series of bismuth – based catalysts, selective for the CO_2 electro-reduction to formic acid, with theoretically enhanced structural stability due to the addition of a carbon shell to prevent the particle degradation at high temperature or high current densities for long-term experiments.

1. Development of the new catalysts series

New bismuth-based catalysts were synthesized using the experimental procedure studied by different research teams for tin-based catalysts [23] [24] [26] [27].
Eight different catalysts were obtained using different precursors from the original synthetic route except for routes [25] and [28], already specific for bismuth.

Table 2 *Synthetic routes used for developing the new bismuth-based catalysts.*

Synthetic route	New precursor	Structure expected
[23]	$NaBiO_3$	Pomegranate Bi_2O_3 and Bi_2O_3@C
[24]	$Bi(AOC)_3$	Nanocomposites Bi_2O_3 and Bi_2O_3@C
[25]	$Bi(NO_3)_3$	Bismuth nanorods – nitrogen doped@C nanotubes
[26]	$NaBiO_3$	Mesoporous nanochains Bi_2O_3@C
[27]	$BiCl_3$	Microporous composites Bi_2O_3@C
[28]	$BiCl_3$	Sulfur doped bismuth nanoparticles

As Table 2 shows, the synthesis of the *Pomegranate* and *Nanocomposites* structured catalysts, have been performed for two different products each, one containing the carbon shell, and the other, without.

1.1 Synthesis of the pomegranate Bi_2O_3 and Bi_2O_3@C

1.1.1Materials

The chemicals cited next were used as received without further purification: D-glucose (anhydrous, biotechnology grade, VWR Life Science), ethanol (99,8 %, abs. p., Chem-Lab), Sodium bismuthate (ACS, 80% min, Thermo Scientific Chemicals).

1.1.2 Synthesis

The Bi_2O_3 and Bi_2O_3@C catalysts were obtained through hydrothermal synthesis using the synthetic route discovered by W. Wena et al. [23] readapted for bismuth.
10 mmol of sodium bismuthate were dissolved in 50 mL of 1 M glucose aqueous solution, poured into a 100 mL Teflon-lined stainless steel autoclave, and heated at 180 °C for 4 hours. The precipitates were collected and washed several times with

water and ethanol. After drying overnight at 80°C, the Bi_2O_3 and Bi_2O_3@C powder products were obtained after annealing into a tube furnace at 550°C for 4 hours with a heating rate of 2 °C min^{-1} in air and argon atmosphere, respectively.

1.2 Synthesis of the nanocomposites Bi_2O_3 and Bi_2O_3@C

1.2.1 Materials

Bismuth acetate (99,99%, Thermo Scientific Chemicals).

1.2.2 Synthesis

Bi_2O_3 and Bi_2O_3@C nanocomposites were obtained by weighting 5 mmol of bismuth acetate and heating it at 550 °C in a tube furnace with a heating rate of 5 °C min^{-1} and keeping the sample at the target temperature for 3 hours in air and argon atmosphere, to obtain Bi_2O_3 and Bi_2O_3@C, respectively.

1.3 Synthesis of the bismuth nanorods–nitrogen doped nanotubes

1.3.1 Materials

Glycerol (molecular biology grade, Thermo Scientific), bismuth (III) nitrate pentahydrate (ACS reagent, 98%, Sigma Aldrich), sodium hydroxide (ACS reagent, 98%, pellets, Sigma Aldrich), sodium thiosulfate (ACS reagent, 99%, Sigma Aldrich), L-cysteine (from a non-animal source, BioReagent, suitable for cell culture, ≥98%, Sigma Aldrich), resorcinol (ACS reagent, ≥99,0%, Sigma Aldrich), ethanol (99,8 %, abs. p., Chem-Lab), ammonium hydroxide (ACS reagent, 28.0-30.0% NH_3 basis, Sigma Aldrich), and formaldehyde (ACS reagent, 37 wt. % in H_2O, contains 10-15% Methanol as a stabilizer, Sigma Aldrich).

1.3.2 Synthesis

The first step of the synthesis developed by Wenjun Zhang et al. [25], requires to produce the precursor Bi_2S_3 by dissolving in 20 mL of deionized water and 40 mL of glycerol, 1,46 g of $Bi(NO_3)_3 * 5H_2O$, 4,80 g of NaOH and 0,95 g of $Na_2S_2O_3$.

The solution was transferred into a 100 mL Teflon-lined stainless steel autoclave heated at 160 °C for 20 hours. The precipitates floating on the solution were then collected by centrifugation and washed several times with deionized water, while the rest of the solution was discarded. The precipitates were dried overnight at 60 °C.

100 mg of the obtained precursor, was dispersed in 10 mL of deionized water under ultra-sonication. Then, 10 mg of L-cysteine, 21 mg of resorcinol, 4,38 mL ethanol and

25 µL of ammonium hydroxide were sequentially added to the above mixture under stirring at 40 °C for 30 minutes. Finally, 25 µL of formaldehyde was added dropwise into the dispersion and after which the solution was kept stirring at 40 °C for 6 h to coat a thin shell of resin on the surface of the precursor. Then, the formed product was washed again with water and ethanol and dried overnight at 60 °C.

Finally, the obtained solid was calcined in a tube furnace at 350 °C in air condition with a heating rate of 5 °C min^{-1} for 2 hours and then heated to 600 °C under Ar-H_2 5% for 3 hours.

1.4 Synthesis of the mesoporous nanochains Bi_2O_3@C

1.4.1 Materials

D-glucose (anhydrous, biotechnology grade, VWR Life Science), ethanol (99,8 %, abs. p., Chem-Lab), Sodium bismuthate (ACS, 80% min, Thermo Scientific Chemicals).

1.4.2 Synthesis

Bi_2O_3@C mesoporous nanochain was prepared by simple hydrothermal method readapting the synthetic route used by Guoen Luoa et al. [26]. 0,850 g of sodium bismuthate was weighted and dissolved in an aqueous solution of 12 g of glucose in 100 mL of water. The solution was transferred in a 100 mL Teflon-lined stainless steel autoclave, sealed, and kept at 180 °C for 4 hours in an oven prior to cool down to room temperature. The precipitates were harvested and washed several times with ethanol and water before being dried overnight at 80 °C.

1.5 Synthesis of the microporous composites Bi_2O_3@C

1.5.1 Materials

Bismuth(III) chloride (anhydrous, powder, 99,998% trace metals basis, Sigma Aldrich), D-glucose (anhydrous, biotechnology grade, VWR Life Science), ethanol (99,8 %, abs. p., Chem-Lab), and Pluronic F127 (powder, bioreagent, Sigma Aldrich).

1.5.2 Synthesis

In the readapted method of Ming-Shan Wang et al. [27], the first synthetic step started by dissolving 1 g of $BiCl_3$ in 50 mL of deionized water under stirring for 30 minutes. The clear solution was transferred into a 100 mL Teflon-lined stainless steel autoclave,

followed by heating in an oven at 120 °C for 24 hours. Then the Bi_2O_2 precipitates were harvested by centrifugation and washed with water and ethanol several times.
0,6 grams of the obtained precursor were dispersed in an aqueous solution of glucose and pluronic F127 prepared by dissolving 6 g of the former and 0,56 g of the latter into 60 mL of deionized water. The suspension was kept stirring for 30 minutes before being transferred into a 100 mL Teflon-lined stainless steel autoclave at 180 °C for 6 hours. The precipitates were collected by centrifugation, washed several times with water, and dried overnight at 60°C. The product was then calcined in a tubular furnace at 420 °C for 30 minutes under air atmosphere, to obtain a porous structure followed by annealing of the catalyst at 550 °C for 5 hours under argon flow.

1.6 Synthesis of the sulfur doped bismuth nanoparticles

1.6.1 Materials

Bismuth(III) chloride (anhydrous, powder, 99,998% trace metals basis, Sigma Aldrich), DMF (Anhydrous, 99.8%, Sigma Aldrich), thioacetamide (ACS reagent, ≥99.0%, Sigma Aldrich), and ethanol (99,8 %, abs. p., Chem-Lab).

1.6.2 Synthesis

The sulphur-doped bismuth nanoparticles synthesis developed by Wenchao Ma et al. [28] adopted in this work started by dissolving in 80 mL of DMF, 1,32 mmol of $BiCl_3$ and 6,01 mg of thioacetamide. The solution was stirred 30 minutes and transferred into a 100 mL Teflon-lined stainless steel autoclave heated at 180 °C for 24 hours, the product was then collected by centrifugation and washed with water and ethanol, and ultimately dried overnight at 60 °C.

2. Optimization of the reactor back pressure

2.1 Materials

Bismuth(III) oxide 90-210 nm (ReagentPlus®, powder, 10 µm, 99.9% trace metals basis, Sigma Aldrich), NAFION® solution (Ion Power), ethanol (99.8 %, abs. p., Chem-Lab), potassium hydrogen carbonate (99.5+%, v.p., Chem-Lab), potassium hydroxide (85+%, pellets a.r., Chem-Lab), propanol-2 (99.8+%, iso-propanol a.r., Chem-Lab).

2.2 Experimental procedure

The optimal back pressure within the flow-by catholyte reactor adopted in this work was determined in two steps.

At first, the valve used to regulate the pressure was studied by determination of the pressure correlated to each valve set point using a digital pressure indicator. In this phase, instead of using a GDE in the cathodic compartment, an aluminium layer of 1 cm^2 surface area was used to separate the liquid from the gas flow, to better identify the pressure on both sides. The reactor's feeds were kept flowing as usual at 2 mL min^{-1} for the liquid electrolytes, and 15 mL min^{-1} for the CO_2 stream, the reactor was heated in an oven at 85 °C during the whole experiment, while the pressure was determined for each set point analysed.

In the second step, once a linear region between the opening of the valve and the pressure measured by the digital indicator was determined, several 24-hour chronopotentiometry experiments at 85 °C have been performed using an Ametek PARSTAT 3000A potentiostat. The conditions used for the analysis were as follow:

- Reference catalyst: commercial bismuth(III) oxide 90-210 nm purchased from Sigma Aldrich, used by spray coating on a GDE about 25 cm^2 of area then cut in a small GDE about 1 cm^2 of area and placed in the electrolyzer.
- Current density of -100 mA cm^{-2} was carried at the same reactor condition as the first step.
- Different back pressure values for each experiment.

These different performed tests, allowed to observe a trend between the faradaic efficiency of the catalyst and the applied back pressure applied, revealing a maximum point at the optimal back pressure.

3. Physiochemical characterization

3.1 Nitrogen adsorption/desorption at -196°C

The determination of the surface area of the catalysts is based on the Brunauer-Emmet-Teller (BET) multi-point method [21]. This method requires the use of a gas, such as nitrogen or argon, which physically adsorb on the surface of the catalysts. By measuring the difference between the pressure of the ingoing gas and the pressure of the outgoing flow, it is possible to determine the quantity of gas adsorbed on the surface. Using the BET equation:

$$\frac{1}{W\left(\left(\frac{P^0}{P}\right)-1\right)} = \frac{1}{W_m C} + \frac{C-1}{W_m C}\left(\frac{P}{P^0}\right)$$

Where:

- W is the mass of the adsorbed gas at the relative pressure;
- P/P^0 is the relative pressure of gas;
- W_m is the weight of the adsorbate constituting a monolayer of coverage;
- C is the BET factor and consists in the difference between the energy of the physical adsorption of the monolayer and the adsorption of subsequent multilayers.

It is possible to plot a linear range between $1/W((P^0/P)-1)$ and (P/P^0), which leads to calculating the weight of gas adsorbed on the catalyst monolayer W_m using the slope and intersection of the BET equation:

$$Slope = \frac{C-1}{W_m C}$$

$$Inter. = \frac{1}{W_m C}$$

and ultimately the total surface area:

$$Surface\ area = \frac{W_m N A_{cs}}{M}$$

Where:

- N is Avogadro's number
- A_{cs} is the cross-sectional area of the adsorbate molecule
- M is the molar mass of the adsorbate employed

The specific surface area can finally be calculated by the surface area previously obtained by dividing it by the mass of the sample used (w):

$$Specific\ Surface\ area = \frac{Surface\ area}{w}$$

The determination of the porosity is made by correlating the type of isotherm observed during the analysis. The IUPAC published in 1985 the classification of six different type of adsorption isotherms.

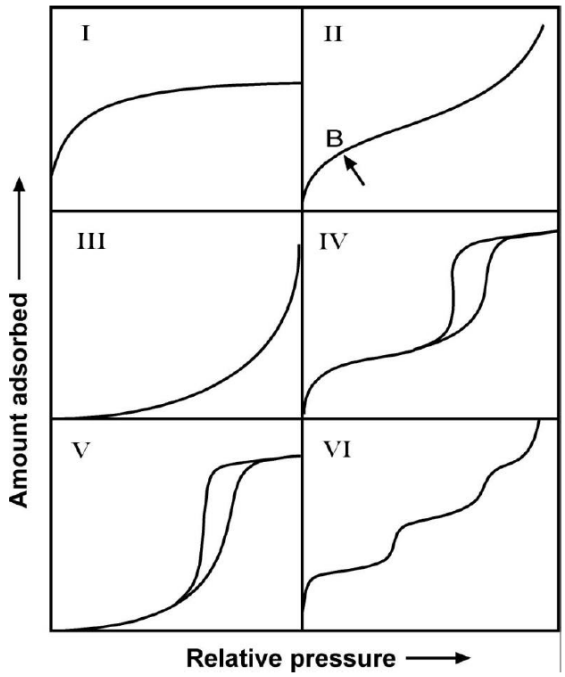

Figure 18 *IUPAC classification of adsorption isotherms curve [21].*

Type 1 is characteristic of microporous catalysts with a size regime <2 nm.

Type 2 adsorption isotherms are typically obtained for macroporous or non-porous adsorbent with a size regime >50 nm [21].

Type 3 isotherms are uncommon, an example of this type of sorption is the nitrogen adsorption on polyethylene [21].

Type 4 isotherms are typical of mesoporous adsorbent with a size regime >2nm <50 nm.

Type 5 differs from the type 4 adsorption isotherm for the stating trend, its curve lies between a type 3 and a type 4.

Type 6 isotherm is a special case representing a step-wise multilayer adsorption on a uniform non-porous surface [21].

Experimental Procedure

Nitrogen (N_2) physisorption was performed at -196°C K with a Quantachrome Quadrasorb SI (Quantachrome Instruments, Boynton Beach, FL, USA) automated surface area & pore size analyser. Prior to the measurements, all samples were degassed for 16 h at 200 °C. The specific surface area was calculated using the Brunauer-Emmet-Teller (BET) equation. The pore diameter considered for each catalysts was the maximum distribution calculated between the pore size diameter and

ratio between the differential value of the pore volume and the differential value of the pore diameter, using the desorption curve values.

3.2 X-ray diffraction

X-ray diffraction is a powerful method to characterize the crystallinity of a solid. The analysis is based on the diffraction of the X-ray beam on the sample surface, when the radiation encounters the crystalline surface, it is elastically scattered in all directions, but depending on the different crystalline planes, one direction, in particular, maintains a high intensity comparable with the source radiation. Bragg reflection's law allows to determine, based on the wave length **λ** and the angle of incidence of the X-ray source **θ**, the interplanar space **d** between adjacent lattice planes, which leads to the characterization of the analysed solid.

$$\lambda = 2d \sin\theta$$ *Bragg reflection's law*

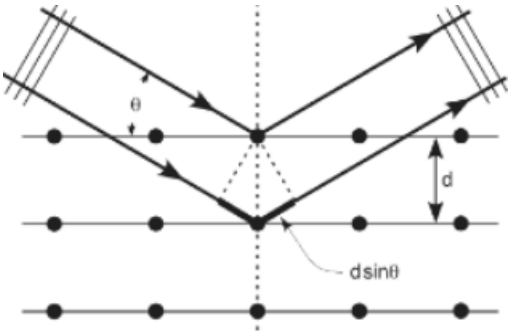

Figure 19 *Bragg's law explanation.*

Experimental procedure

XRD was measured on a Bruker D8 ECO powder diffractometer with a LYNXEYE XE−T detector and Cu K-Alpha radiation. All samples were scanned from 0–80° 2θ and compared with the crystallography open database.

3.3 Scanning electronic microscope (SEM)

SEM microscopy is generally used to determine the surface structure of a solid, with a maximum resolution of 10-50 Å. The principle behind this method is based on using a beam of electrons with a diameter of 5-10 nm to irradiate the sample surface. The primary electrons will be back scattered from the sample surface resulting in secondary emissions such as Auger electrons, secondary X rays and Cathode-luminescence. Depending on the morphology of the material the sum of all these phenomena will lead to the 3D imagine of the surface structure.

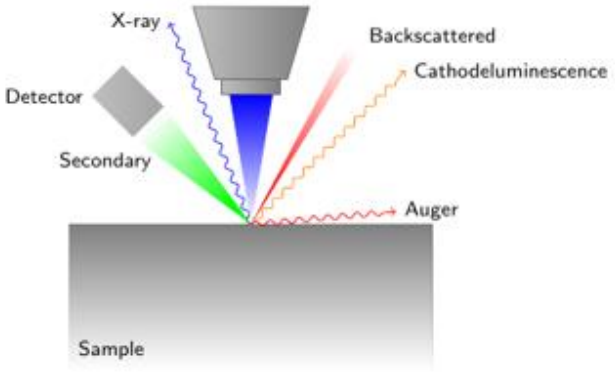

Figure 20 *Secondary emission during SEM determination.*

Experimental procedure

SEM measurements were carried out using a ThermoFisher Scientific Quanta FEG 250.

3.4 Thermogravimetric analysis

Determination of weight loss over a certain temperature range can be performed by thermogravimetric analysis (TGA), in which the sample is placed in a crucible on a heated balance inside a furnace that can reach high temperatures. The system is saturated with different gases depending on the conditions of the analysis; a fume hood is used to control the atmosphere inside the furnace. The test makes it possible to determine critical information such as the degradation temperature of a material, the inorganic and organic percentage of the sample, the starting temperature for any structural change leading to weight loss, etc.

TGA is widely used in the polymer field to determine glass transition and degradation temperature and mechanism. In this project, it was essentially used to determine the percentage of carbon introduced during synthesis in the catalysts studied. The determination of the percentage of carbon was possible by observing, the difference in weight between the start and finish temperature, as the carbon will be converted to CO_2 at high temperatures and in an oxidizing atmosphere.

Experimental procedure

TGA analyses were performed using a thermo-gravimetric balance TA Q5000 IR. Each synthesized catalyst was investigated from 0 to 800 °C under air atmosphere.

3.5 Inductively coupled plasma – mass spectrometry

ICP – MS is a powerful technique to quantitatively determine the concentration of elements in a sample. It is particularly used for the determination of metals. The method uses a plasma generated by the excitation of a gas (generally argon) by the magnetic field induced by a variable electric field applied using a current flow within a toroidal solenoid. The excited gas, emits electrons that are directed by the magnetic field forming the plasma. The torch reaches around 5000-6000 K and is cooled outside by a cooling gas. The sample is introduced into the plasma as a liquid before being atomized and converted into polyatomic ions which are then detected by mass spectrometry.

In this project ICP-MS was used to determine the percentage of bismuth in the synthesised catalyst and to more accurately determine by difference, the percentage of carbon within the sample.

Experimental Procedure

ICP-MS analyses were possible using an Agilent 7500 ICP-MS. The determination of bismuth in all catalysts was investigated by constructing a linear regression in range of concentrations between 100 ppb and 10 ppm, using a metallic bismuth reference. Each catalyst was previously digested with 70% nitric acid (ChemLab) and then diluted to the proper concentration.

4. LSV and CV experiments of the synthesized catalysts

4.1 Linear sweep voltammetry

Linear sweep voltammetry or LSV is an electrochemical technique used to study the electrochemical behaviour of a substance in a determined range of potential. In electrochemistry, two different types of current can be observed, the faradaic current and the capacitive current. While the former is obtained due to an oxidation or reduction reaction involving the sample under analysis at a specific potential value, the latter is always present as a consequence of the double layer on the electrode surface formed by charged species attracted to the electrode surface under an applied potential. The higher the absolute value of potential, the higher the capacitive current caused by the movement of charged ions to form the double layer. In a classic LSV experiment, the sample is placed in a three-electrode set-up, on the working electrode, while the

potential is read between the working and the reference electrode, the current is measured between the counter and the working electrode. Using this technique, a lot of information can be obtained regarding the electrochemical activity of the sample in the chosen environment conditions in the used potential range. LSV experiments are usually performed under steady-state conditions without stirring, where mass transport is the limiting phenomenon instead of electron transfer.

Under this condition, the system is considered reversible and the Randles-Sevcik equation applies:

$$I = 0.4463\, nFA \left(\frac{nF}{RT}\right)^{\frac{1}{2}} D^{\frac{1}{2}}\, v^{\frac{1}{2}}\, C \qquad \textit{Randles-Sevcik equation}$$

Where:

- I is the faradaic current intensity
- n is the number of electrons exchanged in the reaction
- F is the Faraday constant
- R is the ideal gas constant
- D is the diffusion contant
- v is the scan rate adopted in the experiment
- C is the anolyte concentration in the system

Based on this equation, using the linear correlation between the square root of the scan rate or the square root of the diffusion coefficient and current intensity measured, the potential value at which the faradaic peak is observed, qualitative and quantitative measurements are possible for example to determine the concentration of analyte in a solution or the chemical species under analysis.

4.2 Cyclic voltammetry

Cyclic voltammetry is a technique similar to LSV, where instead of scanning from a starting potential to a final potential just in the cathodic or anodic potential range, the potential is scanned cyclically, leading to cathodic and anodic peaks based on the reduction and oxidation reaction of the sample under analysis. Cyclic voltammetry is used even for other applications such as the deposition of electrochemically active sensors on the electrode surface.

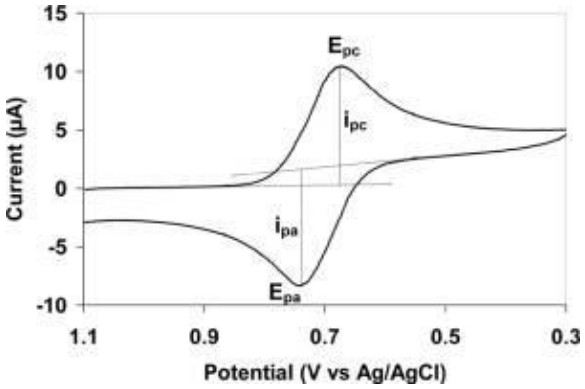

Figure 21 *Example of voltammogram.*

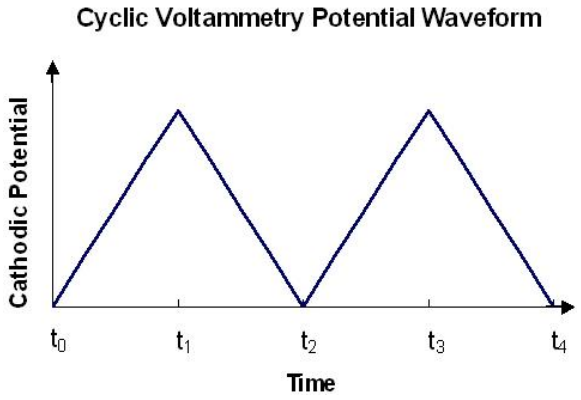

Figure 22 *Waveform of the potential applied during two scans of CV.*

Cyclic voltammetry is commonly used at high scan rate values, in order to determine the overall behaviour in a large potential range analysed. Differently, LSV is used at lower scan rate than CV to focus on the interested potential window, and determine more accurately the electrochemical response of the target material.

4.3 Materials

NAFION® solution (Ion Power), propanol-2 (99.8+%, iso-propanol a.r., Chem-Lab), Bismuth(III) oxide 90-210 nm (ReagentPlus®, powder, 10 µm, 99.9% trace metals basis, Sigma Aldrich), potassium hydrogen carbonate (99.5+%, v.p., Chem-Lab).

4.4 Experimental procedure

The electrochemical activity of each synthesized catalyst was tested by LSV and CV methods using a Metrohm VIONIC potentiostat and a three-electrode set up in a single-compartment cell. A rotating disk of glassy carbon and a glassy carbon stick electrodes were used as working and counter electrodes, respectively. A saturated Ag/AgCl electrode was used as a reference. The working electrode was kept rotating, to limit the bubble formation during the experiment and the resulting increase in resistance.

The overall configuration was placed in a Faraday cage to isolate the background noise.

The catalysts were fixed on the working electrode by drop casting method of a solution previously prepared by dissolving 10 mg of the catalyst in 300 µL of isopropanol alcohol and 54 µL of Nafion solution. The loading of catalysts on the electrode surface was 0,250 mg cm^{-2} for each measurement.

An aqueous solution of potassium hydrogen carbonate 0,5 M was prepared and used as electrolyte solution.

Each measurement performed consisted of a five cycles cyclic voltammetry test followed by a linear sweep voltammetry test, each catalyst was measured both in a nitrogen-saturated solution and a carbon dioxide-saturated solution.

CV experiments were performed in a potential range from +0,8 to -2,2 V referring to the open circuit potential (OCP), five times, with a scan rate of 50 mV s^{-1}, while the rotating disk spinning was maintained at 300 rpm.

The LSV experiments were performed at a scan rate of 5 mV s^{-1}, in the potential range between 0 and -2,2 V referring to the Ag/AgCl reference electrode potential. The rotating disk was kept spinning at 300 rpm.

Overall conditions illustrated in Table 3.

Previous analyses were performed using 80% of positive feedback IR drop compensation. After comparing the experimental results with and without the compensating potential it has been decided to avoid the use of a compensating current since the results obtained didn't differ significantly.

Table 3 *Summary of CVs and LSVs experiments conditions.*

Working electrode	Glassy carbon
Reference electrode	Ag/AgCl
Counter electrode	Glassy carbon
Electrolyte	$KHCO_3$ 1M
Catalyst's loading	0,250 mg cm^{-2}
CV's potential range	From + 0,8 to - 2,2 V ref. OCP
CV's scan rate	50 mV s^{-1}
LSV's potential range	From 0 to - 2,2 V ref. Ag/AgCl
LSV's scan rate	5 mV s^{-1}

5. ECSA determination

The specific surface area is a different parameter than the electrochemical active surface area (ECSA), which is a main factor in describing and comparing different electrocatalysts.

ECSA is defined in terms of capacitance, thus, the quantity of charge that a specific catalyst can store at a defined potential. In essence, the ECSA is the portion of the specific surface area, able to exchange and conduct electrons to the adsorbate on the catalyst surface.

The determination of this parameter can be handled using several methods, one of the most common, and also the one adopted in this project, is the determination of the Helmholtz double layer capacitance (DLC) using a differential capacitance measurement (DCM) [22].

This method consists in using a narrow potential range where no faradaic current is observed, in this potential window several scans with increasing scan rates are performed on the catalysts attached to the electrode. When no faradaic current is present, the contribution of capacitive current is 100%, due to the presence of the Helmholtz double layer on the catalysts surface fixed on the electrode. Increasing the intensity of the scan rate will lead to a linear correlation between the observed intensity of the capacitive current and the adopted scan rate, the slope of the linear regression as the following equation shows, defines the relative capacitance C_{DL} of the catalyst:

$$C_{DL} = \frac{\partial Q}{\partial \varphi}$$

$$I = \frac{\partial Q(\varphi)}{\partial t}$$

$$I = C_{DL}\frac{\partial \varphi}{\partial t}$$

Where:

- Q is the charge;
- Φ is the potential;
- I is the current intensity;
- dΦ/dt is the scan rate.

ECSA can be calculated by dividing the relative capacitance calculated by the double-layer measurement, by the specific capacitance of the target element that considers the mass of the sample involved:

$$ECSA = \frac{C_{DL}}{C_S}$$

5.1 Materials

Bismuth(III) oxide 90-210 nm (ReagentPlus®, powder, 10 µm, 99.9% trace metals basis, Sigma Aldrich), NAFION® solution (Ion Power), ethanol (99.8 %, abs. p., Chem-Lab), potassium hydrogen carbonate (99.5+%, v.p., Chem-Lab), potassium hydroxide (85+%, pellets a.r., Chem-Lab), propanol-2 (99.8+%, iso-propanol a.r., Chem-Lab).

5.2 Experimental procedure

The electrochemical active surface area was determined using a catholyte flow-by reactor configuration heated in an oven at 85 °C with a CO_2 gas feed of 15 mL min^{-1} and an electrolyte flow of 2 mL min^{-1} (0,5 M $KHCO_3$ as the catholyte and 2 M KOH as the anolyte). The working electrode consisted of a GDE, spray-coated with the synthesized catalysts using an ink made by suspending 0,075 g of the catalyst in 0,375 g of nafion solution, 4,875 g of isopropanol alcohol, and 4,875 g of deionized water.
The overall loading was 2 mg cm^{-2}.
The electrochemical active surface area determination was performed by Helmholtz double layer capacitance (DLC) using a differential capacitance measurement (DCM). For each catalyst, several cyclic voltammetry tests were done with an Ametek PARSTAT 3000A potentiostat, using different scan rates such as 80, 120, 160, 200, 240, 280, 320 mV s^{-1} in a potential window of ± 0,050 V referring to the OCP. The capacitance current was calculated by subtraction between the anodic and the cathodic current in a central position of potential.

6. Chronopotentiometry tests of the new series of catalysts

Chronopotentiometry is an electrochemical measurement of the potential response at a defined value of current intensity. In this project, chronopotentiometry was applied to convert CO_2 to formic acid, supplying a constant current density value of -100 mA cm^{-2}, while the cell potential was measured throughout the experiment. Chronopotentiometry is the opposite experiment of chronoamperometry, where instead, a constant potential is applied, and the current value is measured during the experiment. Since the electrolyzer configuration used in this design is the flow-by catholyte reactor type, the supply of reactants is continuous and the concentration of

CO_2 in the double layer near the surface of the catalysts is kept constant at the maximum point set by its solubility according to Henry's constant for the electrolyte solution used. The turbulence flow on the working electrode surface acts as an agitator, leading to the continuous replacement of the CO_2 converted to formic acid.

For this reason, the potential value observed during the analysis is mostly constant, with variations during the experiment due to bubbles or changes in the components of the set-up such as the membrane or the catalyst.

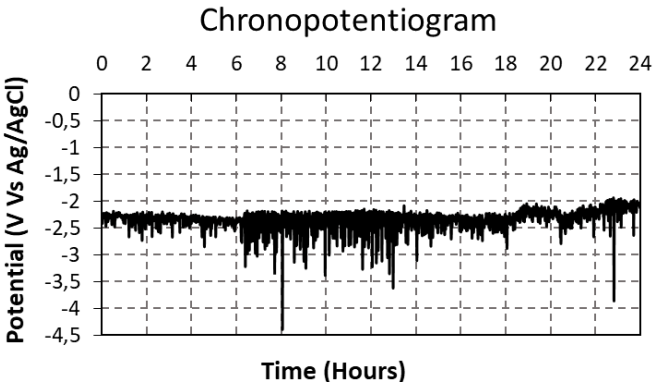

Figure 23 *Example of chronopotentiogram obtained by measuring the potential of the working electrode versus an Ag/AgCl reference electrode for a 24-hour experiment with 100 mA cm^{-2} as current density.*

Current interrupt is an electrochemical technique used to determine the total resistance of an electric system. This method is based on applying a specific potential for a few seconds and quickly dropping it to zero. The current is measured for the overall duration of the experiment. According to Ohm's law:

$$V = IR$$

The total resistance R_Ω of the system is calculated by:

$$R_\Omega = \frac{V_1 - V_2}{I_1}$$

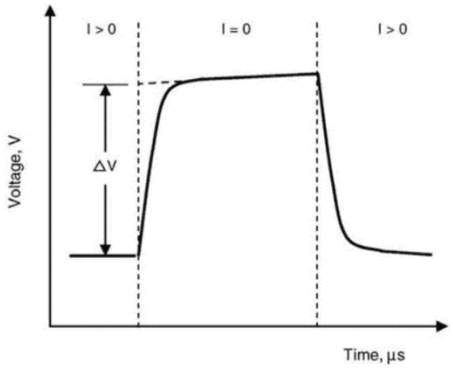

Figure 24 *Ideal voltage waveform during current interrupt event.*

According to this method, it is possible to consider the resistance of the system caused by the electrolyte, and electrodes, also defined as ohmic resistance.
To balance this resistance, the equilibrium potential needed for the target reaction requires the addition of an over-potential called ohmic over-potential:

$$\Delta^{\neq}G = \Delta^{\neq}G^{0} + \boldsymbol{\alpha F \Delta\varphi}$$

Where:

- $\Delta^{\neq}G$ is the Gibbs energy of the system required to perform the chemical reaction;
- $\Delta^{\neq}G^{0}$ is the Gibbs energy at the equilibrium for the reaction and its reverse reaction;
- α is the charge transfer coefficient and it signifies the fraction of the interfacial potential at the electrode-electrolyte interface that helps in lowering the free energy barrier of a reaction. It has significance related to the kinetic of the reaction since it is a measure of the rate at which the electron transfer occurs between the interface electrode-electrolyte;
- F is the Faraday constant;
- Δφ is the potential added to the equilibrium.

6.1 Materials

NAFION® solution (Ion Power), propanol-2 (99.8+%, iso-propanol a.r., Chem-Lab), Bismuth(III) oxide 90-210 nm (ReagentPlus®, powder, 10 μm, 99.9% trace metals basis, Sigma Aldrich), potassium hydrogen carbonate (99.5+%, v.p., Chem-Lab).

6.2 Experimental procedure

The newly synthesized series of catalysts were tested on three different levels by chronopotentiometry tests. The reactor set-up used, consisted of a catholyte flow-by reactor heated at 85 °C, with a water solution of $KHCO_3$ 0,5 M and KOH 2 M as catholyte and anolyte, respectively. The liquid flow was maintained at 2 mL min^{-1} while the gas stream was kept at 15 mL min^{-1}. The working electrode consisted of a 1 cm^{-2} GDE spray-coated with a loading of 2 mg cm^{-2} of the catalyst prepared as mentioned in the paragraph 5.2.

The first stage of measurements consisted in testing the catalysts using a PARSTAT 3000A potentiostat at different current densities such as -50 mA cm^{-2}, -75 mA cm^{-2}, -100 m A cm^{-2}, -125 mA cm^{-2} and -150 mA cm^{-2} for 15 minutes chronopotentiometry tests for each catalyst. The faradaic efficiency was determined for every current density by sampling the electrolyte and determining the formic acid concentration by HPLC

analysis. After calculation of the concentration of formic acid produced, the molar flux is calculated considering the volume of the sample withdraw, and a sampling time of 2 minutes. Then, the molar flux is multiplied by two, which are the electrons exchanged for each CO_2 molecules, and by the faraday constant, to be ultimately divided by the current density used during the analysis.

All catalysts followed the second measurements level, where the samples were analysed at -100 mA cm^{-2} for 6 hours of chronopotentiometry testing at the same reactor conditions as in the first step.

Samples were collected 20 and 40 minutes after the start of the measurement and then 1, 2, 3, 4, 5, and 6 hours after the beginning. The formic acid concentration was determined for each sample to enable the calculation of the corresponding faradaic efficiency at that time.

Finally, the best performing catalysts, were selected and tested for 24 hours at -100 mA cm^{-2} chronopotentiometric tests. Again, the samples were collected 20 and 40 minutes, 1, 2, 3, 4, 5, 6 hours and at 22, 23, and 24 hours after the start of the measurement.

Each measurement level was tested three times for each synthesized catalyst, to collect a more solid and representative sample of data.

Chapter 4

Results elaboration and discussion

The following sections will illustrate and discuss the experiments performed and the results obtained in this work, providing a correct interpretation of the chemical behaviour of the new series of bismuth catalysts.

1. Physiochemical characterization

1.1 Nitrogen adsorption/desorption

The first analysis performed on the new series of catalysts was the determination of the specific surface area, and total pore volume by nitrogen adsorption method at -196 °C with Quantachrome Quadrasorb SI (Quantachrome Instruments, Boynton Beach, FL, USA), using the procedure described in Paragraph 3.1 of Chapter 3. The results determined by this technique are illustrated for each catalyst in Table 4.

Table 4 *Results of surface area and total pore volume for the new series of bismuth catalysts synthesized.*

Catalyst structure	Surface area ($m^2\ g^{-1}$)	Total pore volume ($cm^3\ g^{-1}$)
Pomegranate Bi_2O_3	0,5	$2,2 \cdot 10^{-3}$
Pomegranate Bi_2O_3@C	84,5	$6,4 \cdot 10^{-2}$
Nanocomposites Bi_2O_3	0,3	$7,9 \cdot 10^{-4}$
Nanocomposites Bi_2O_3@C	21,1	$3,4 \cdot 10^{-2}$
Nanorods N-doped	4,3	$1,4 \cdot 10^{-2}$
Mesop. Nanochain Bi_2O_3@C	1,2	$4,6 \cdot 10^{-3}$
Microp. composites Bi_2O_3@C	260,8	$1,6 \cdot 10^{-1}$
S-doped Bismuth nanopart.	2,5	$9,0 \cdot 10^{-3}$

Analysing the surface area values, three structures among all, showed promising data, such as the pomegranate Bi_2O_3@ catalyst, the nanocomposites Bi_2O_3@C catalyst, and the microporous composites Bi_2O_3@C catalyst. Interesting are the results obtained for the latter, due to the similar values obtained by M. S. Wang et al. [27] in the original synthesis performed using a tin-based precursor. In fact, a 272,7 $m^2\ g^{-1}$ surface area and a total pore volume of 0,36 $cm^3\ g^{-1}$ were obtained for the tin catalyst synthesized by M. S. Wang (compared with 260,8 $m^2\ g^{-1}$ and 0,16 $cm^3\ g^{-1}$ obtained in this work). This phenomenon could indicate similar behaviour for tin and bismuth under hydrothermal conditions, and consequent correlations in their structural morphology.
The nitrogen adsorption analysis underlined the role of carbon in increasing the total surface area by separating the bismuth particles, although the measurement is unable to identify and correlate which element between carbon and bismuth is responsible for the observed interaction with nitrogen. To determine the bismuth and carbon

distribution in the catalyst structure, and to determine the overall morphology, SEM analyses were performed.

1.2 Structural characterization by SEM

SEM analyses were performed for the most interesting catalysts based on nitrogen adsorption/desorption data, and previous information given from the original tin-based synthesis. Therefore, the catalysts with the largest surface area, such as the pomegranate Bi_2O_3@ catalyst, the nanocomposites Bi_2O_3@C catalyst, and the microporous composites Bi_2O_3@C catalyst were analysed by SEM microscopy as described in Chapter 3, Paragraph 3.3.

The following reported images 1, 3, and 5, illustrate the microstructures of the three catalysts.

All three catalysts, showed a particle size in the order of micro meters. Each micro-particle catalyst has a different shape and morphology, but all of them showed interesting similarities with the respective tin-based catalyst from the original synthesis.

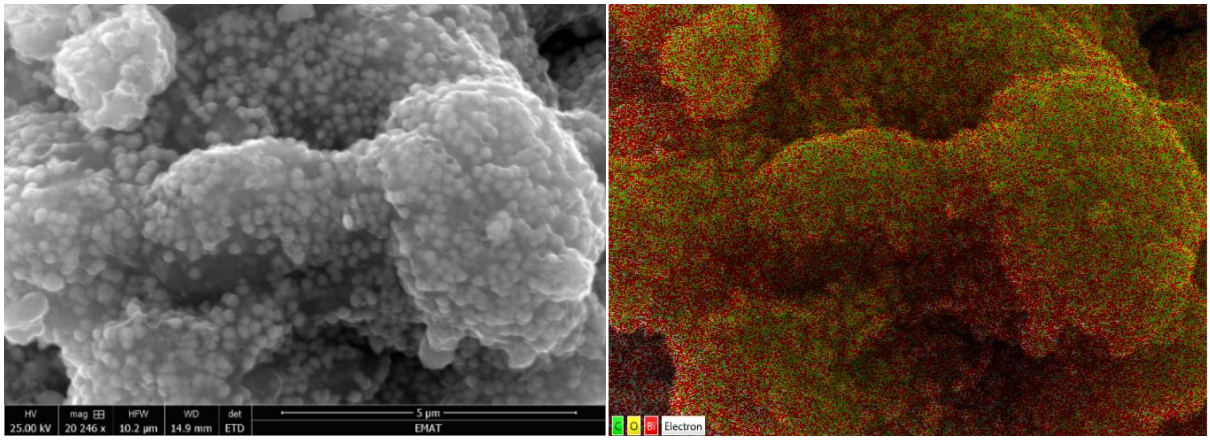

Image 1 *SEM-EDS images of catalyst pomegranate Bi_2O_3@C, magnification 5 µm.*

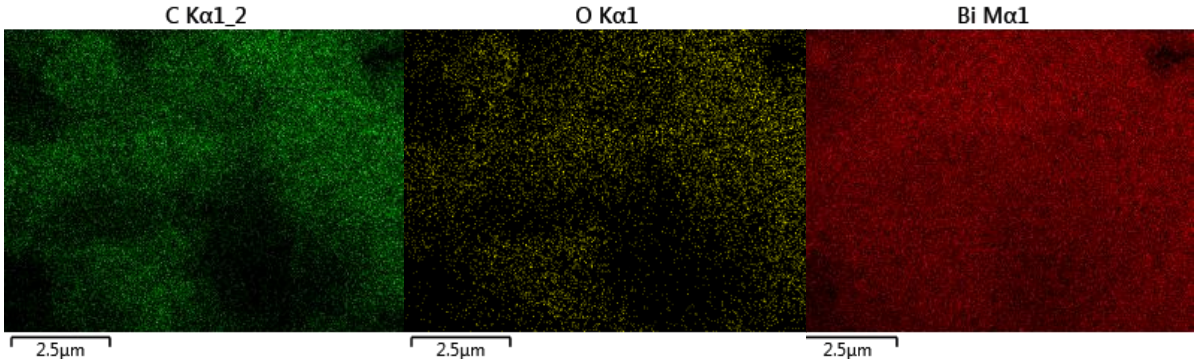

Image 2 *EDS spectra – carbon – oxygen – bismuth distribution, pomegranate Bi_2O_3@C catalyst.*

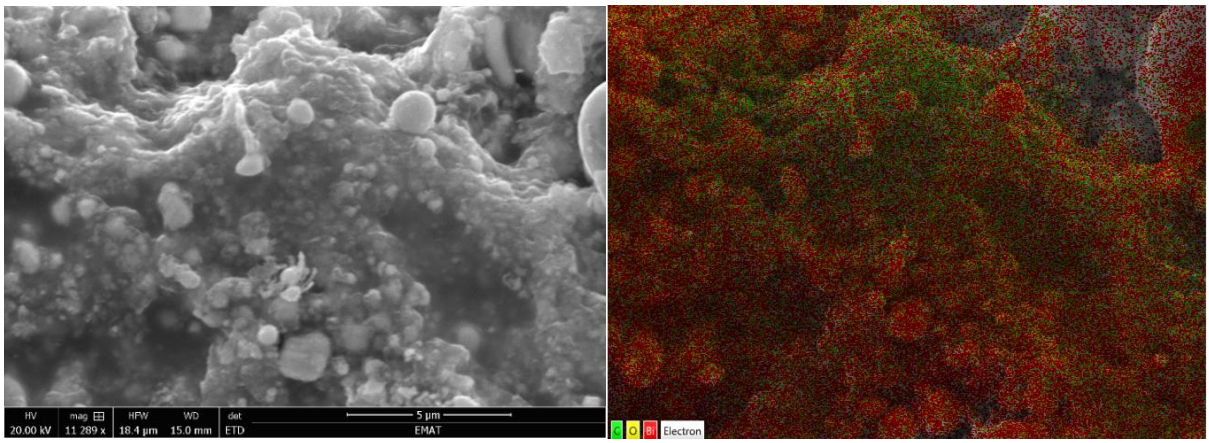

Image 3 *SEM-EDS images of catalyst nanocomposites Bi_2O_3@C, magnification 5 µm.*

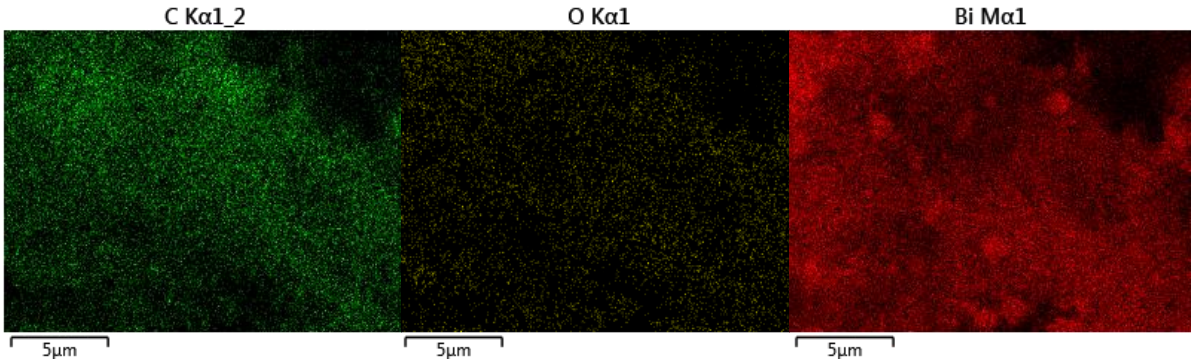

Image 4 *EDS spectra – carbon – oxygen – bismuth distribution, nanocomposites Bi_2O_3@C catalyst.*

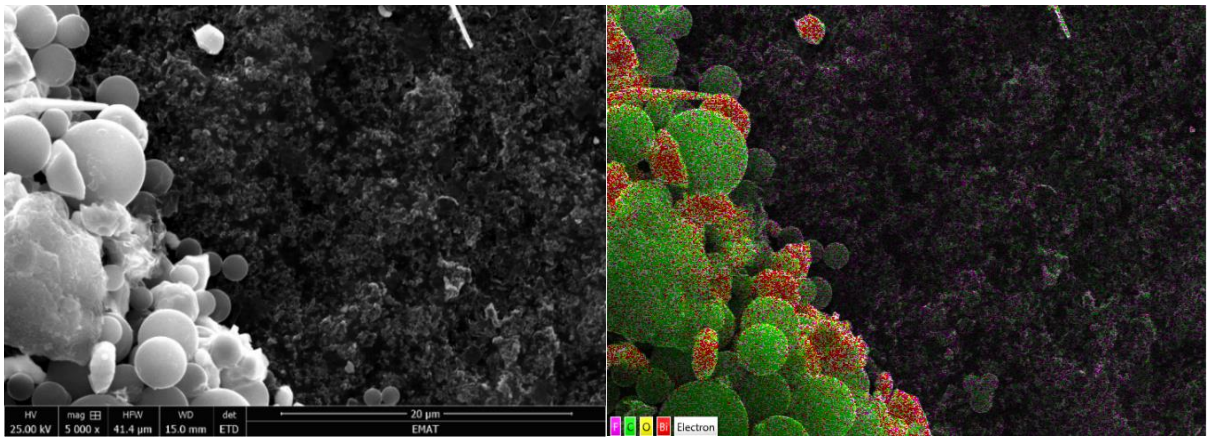

Image 5 *SEM-EDS images of catalyst microporous composites Bi_2O_3@C, magnification 20 µm.*

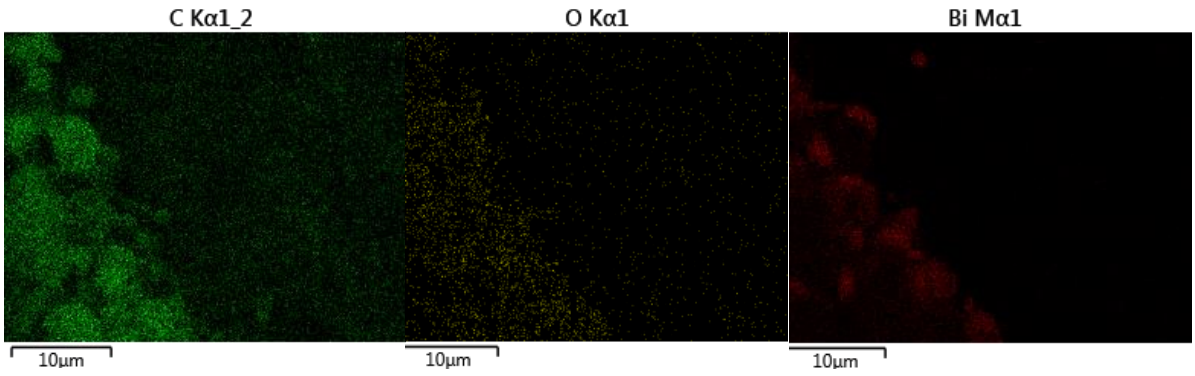

Image 6 *EDS spectra – carbon – oxygen – bismuth distribution, microporous composites Bi_2O_3@C catalyst.*

Observing the SEM data obtained from the work performed in [23], and [27] starting from tin-based precursors, it is possible to correlate the same granular and spherical structure of the pomegranate Bi_2O_3@C and the micro-porous composites Bi_2O_3@C catalysts, to the products obtained in this work in images 1 and 5, respectively. Bismuth appears to behave similarly to tin by hydrothermal synthesis with carbon, as the surface area and structural morphology of the new catalysts are very close to the tin-based version. Although the particle size seems to be different by one order of magnitude, and instead of nanoparticles as expected, only micro-particles were synthesized. The EDS analysis allowed a better understanding of the distribution of the two main elements, bismuth and carbon, within the microstructure. Images 2 and 4, show how their distributions are homogenous for the pomegranate and the nanocomposites catalyst. In contrast, for the microporous composites structure, the spherical carbon micro-particles appear to be completely segregated from the bismuth ones (Image 6). The different carbon distribution around the bismuth micro-particles can influence the performance of the catalyst with two main effects. Firstly, the availability of bismuth could be affected, allowing a greater or lower amount of the substrate to reach the catalyst surface. Secondly, the structural stability can be altered by the presence of more or less diffused carbon between the bismuth particles, leading to long-term or short-term structural stability, respectively.

The correlation between the previous nitrogen adsorption measurement and SEM analyses, shows how the overall surface area can be influenced by the carbon morphology and distribution around the bismuth particles. Spherical segregated carbon particles, for example, could be the main reason for such a great surface area for the microporous composites Bi_2O_3@C catalyst respect to the others. Separation of such particles may enhance the total surface area of both elements, which are more capable of interacting with nitrogen gas.

1.3 XRD analysis

To determine the crystalline domain of the catalysts, XRD analyses were performed. The diffraction patterns of the catalysts are shown in Graph 1.

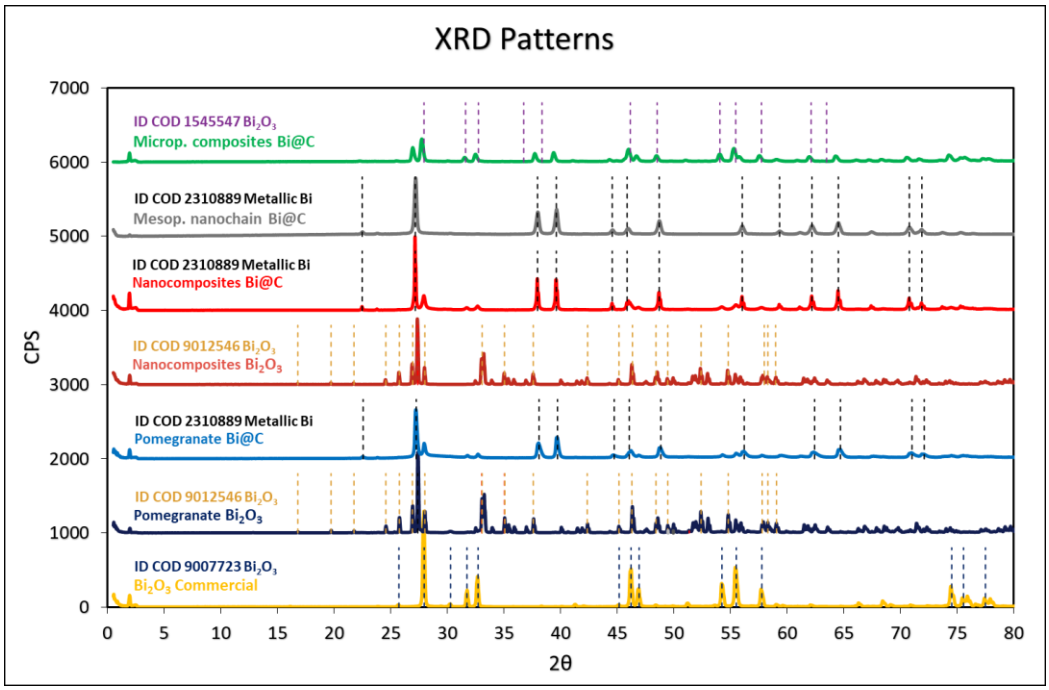

Graph 1 *XRD analysis, all catalysts.*

It is now clear, that not all catalysts have a Bi_2O_3 crystalline structure, as expected from the original synthesis related to tin-based materials. In fact, due to the synthetic method of pomegranate Bi_2O_3@C, nanocomposites Bi_2O_3@C, and mesoporous nanochain Bi@C in which the annealing step was performed in an inert atmosphere, metallic bismuth crystalline structures were obtained. Since the synthesis of the latter is performed without the annealing step, and the crystalline structure is still metallic, it can be deduced, that bismuth differently from tin, under hydrothermal conditions tends to be reduced to its metallic Bi^0 form, so by using a final annealing step in an inert atmosphere rather than in air, the reduced catalyst can be preserved. For example, as the microporous composites Bi_2O_3@C catalyst was subjected to an initial oxidation step in the annealing part for 30 minutes under air atmosphere, the XRD results proved a low percentage match for both the metallic and oxidised crystalline structure, probably caused by the oxidation of part of the catalyst. Catalysts such as pomegranate Bi_2O_3 and nanocomposites Bi_2O_3 subjected to annealing in air conditions, exhibited an oxidized Bi_2O_3 crystalline structure, due to the accelerated oxidation of metallic Bi^0 obtained after hydrothermal conditions to Bi^{3+}, in air at elevated temperatures.

The N-doped nanorods Bi and S-doped Bi catalysts were eliminated from this work because the XRD analysis did not correspond to any known structure in the library used, and because the synthesis performed yielded a very small amount of product. It

was therefore decided to focus on the other catalysts and to continue the characterisation and perform electrochemical tests only on these. As described in Chapter 1, Paragraph 3.4 in the bismuth electrocatalyst section, the influence in the CO_2 conversion by the metallic or oxidized structure of bismuth is still under study. Crystalline lattice determination by XRD will allow a better understanding of the catalysts performance in the last part of this project, where will be possible to compare the selectivity of each catalyst considering their oxidised or metallic structure.
To be correct on the nomenclature used for the synthesized catalysts, a change in their name is essential. The following changes are illustrated in Table 5 and will be observed starting with the beginning of this paragraph.

Table 5 *New catalysts nomenclature.*

Old catalyst structure name	New catalyst structure name
Pomegranate Bi_2O_3@C	Pomegranate Bi@C
Nanocomposites Bi_2O_3@C	Nanocomposites Bi@C

1.4 TGA and ICP-MS analysis

To obtain more information on the quantitative chemical composition of the new catalysts, TGA and ICP-MS analyses were performed. Although, the surface area, morphology, distribution and crystalline structure are known from previous analyses, the total amount of bismuth and carbon in the catalyst is still unknown.
Determining the bismuth – carbon ratio in the new series of catalysts, is useful to predict the possible selectivity, efficiency and activity of the catalysts. Important consideration can also be made on economic aspects since the European Commission declared bismuth a raw material in its communication published in 2020 [29]. Determining the bismuth/carbon ratio in the synthesized structure could lead to a better interpretation of their performances, relying on the different morphology and distribution previously observed by SEM.
The first determination was conducted by TGA analysis, which led to the first, less accurate data, useful for an initial understanding of the amount of carbon within the samples. The results are shown for each catalyst in Table 6.

Table 6 *TGA analysis results.*

Catalyst structure	Carbon percentage % w/w
Pomegranate Bi@C	28,3
Mesop. nanochain Bi@C	74,0
Microp. composites Bi_2O_3@C	46,7

The TGA analysis conducted, yielded information for only three catalysts, since at high temperatures, the oxidation process of metallic bismuth to bismuth oxide, for the nanocomposites Bi@C catalyst structure, led to an increase in weight. The TGA analysis as expected, revealed no weight loss for all the samples without carbon incorporated.

Interesting similarities can be observed by comparing the results obtained by M. S. Wang et al. in their work for the microporous SnO_2 catalyst [27], where the TGA results showed an overall weight loss of 58,2% not that far from the results obtained for the Bi-based version in this work (46,7%).

ICP-MS analyses were performed to obtain more accurate data. The procedure used was previously described in Chapter 3, Paragraph 3.4. The results are illustrated in Table 7.

Table 7 *ICP-MS results.*

Catalyst structure	**Sample weight (mg)**	**Bi conc. (ppm)**	**Carbon weight (mg)**	**Carbon % w/w**
Pomegranate Bi_2O_3	10,2	8,2	-	-
Pomegranate Bi@C	9,0	5,1	3,9	43,3
Nanocomposites Bi_2O_3	10,1	9,1	-	-
Nanocomposites Bi@C	9,6	8,6	1,0	10,4
Mesop. Nanochain Bi@C	10,2	1,6	8,6	84,3
Microp. composites Bi_2O_3@C	10,6	3,5	7,1	67,0

The total carbon percentage was calculated for each carbon-integrated catalyst considering the presence of only metallic bismuth as previously evidenced in the crystalline structures by XRD measurements. Pomegranate Bi_2O_3 and nanocomposites Bi_2O_3 catalysts showed a different bismuth weight from the total sample weight due to the presence of oxygen in the structure.

The observed trend in the ICP-MS measurements is the same as observed by the TGA analysis, as the catalysts followed the same ascending order of carbon percentage as follows:

Mesop. nanochain Bi@C > Microp. Composites Bi_2O_3@C > Pomegranate Bi@C

The obtained data will be used to interpret the performance of each catalyst in the following tests.

2. LSV and CV characterization

LSV and CV analyses were performed to better understand the electrochemical activity of the new electrocatalyst series. The procedure used was previously described in Chapter 3, Paragraph 4.4. The voltammogramms and CVs are shown in Graphs 2 – 13 in this paragraph. Commercial bismuth was analysed as a reference.

The obtained CVs showed an evident difference between the catalysts containing a Bi_2O_3 and metallic Bi^0 crystalline structure. For the catalysts with oxidised bismuth, the reduction and oxidation of Bi^{3+} to Bi^0 and vice versa is very tangible by the peaks observed between -0,4 V and -1,2 V vs Ag/AgCl for the reduction reaction and between -0,4 V and 0,4 V vs Ag/AgCl for the oxidation (Graphs 2, 3, and 4), no significant peaks are observed in the measured potential window for the catalyst with metallic bismuth (Graphs 5, 6 and 7).

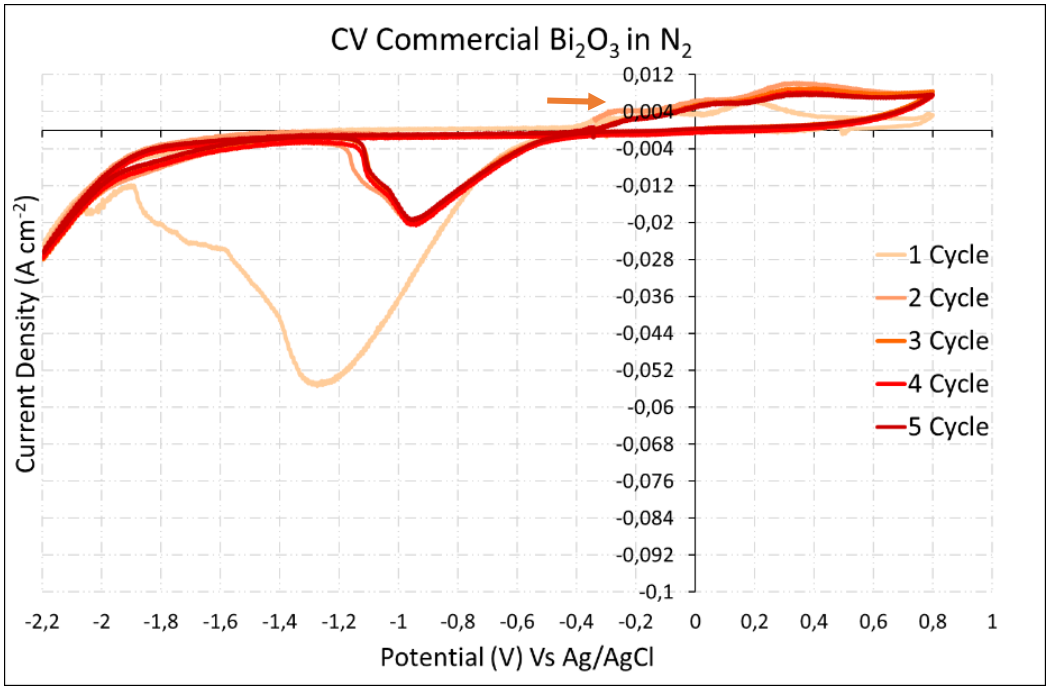

Graph 2 *CV of commercial Bi_2O_3.*

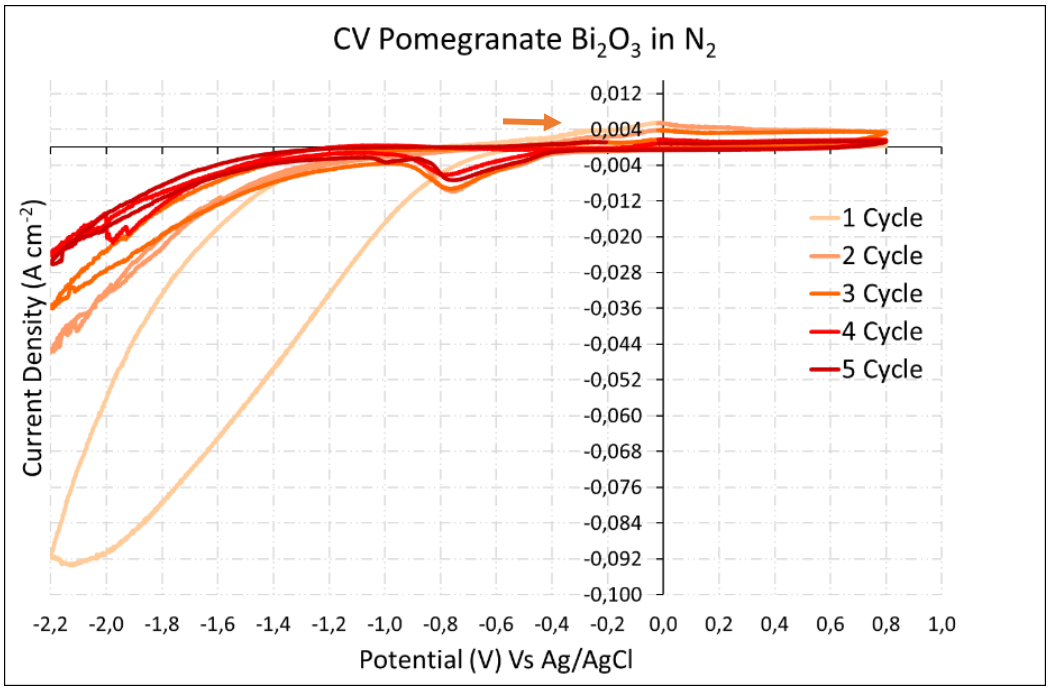

Graph 3 *CV of pomegranate Bi_2O_3.*

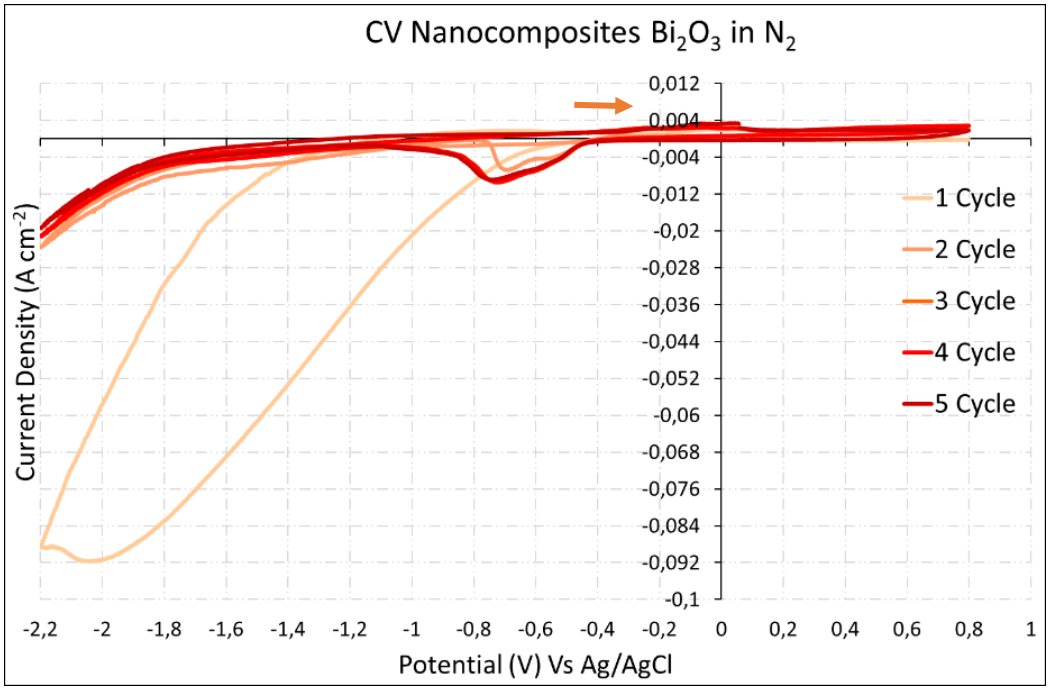

Graph 4 *CV of nanocomposites Bi_2O_3.*

Furthermore, in Graphs 2, 3 and 4, a higher peak in the cathodic potential range can be observed in the first cycle, caused by a higher amount of bismuth oxide present in the catalyst structure at the beginning of the analysis. After the first cycle, the reduction peaks decrease in current density, and probably due to changes in the crystalline structure of the electrocatalysts, the peaks increase in number and shift in potentials. In Graph 3, two cathodic peaks are observed at -0,8 V and -1,0 V vs Ag/AgCl

associated with the reduction of bismuth to different oxidation states, the same behaviour shown in Graph 4 in the potential range between -0,8 V and -0,5 V vs Ag/AgCl.

In Graphs 5, 6, and 7 the only peaks present are caused by the amount of oxidized bismuth present due to spontaneous oxidation of the catalyst by air.

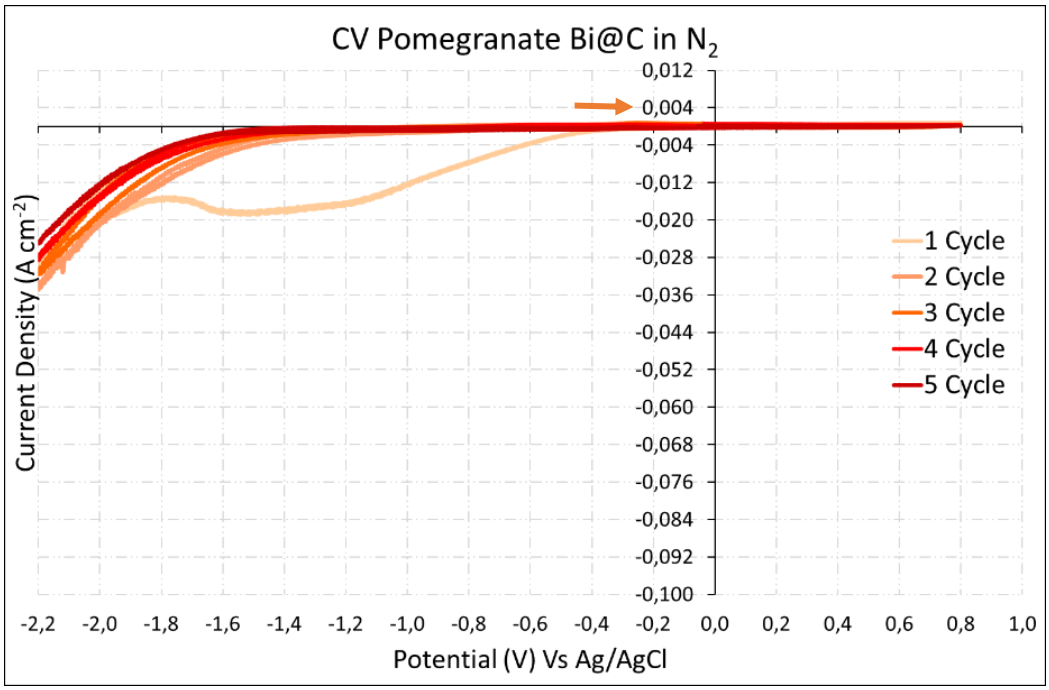

Graph 5 *CV of pomegranate Bi@C.*

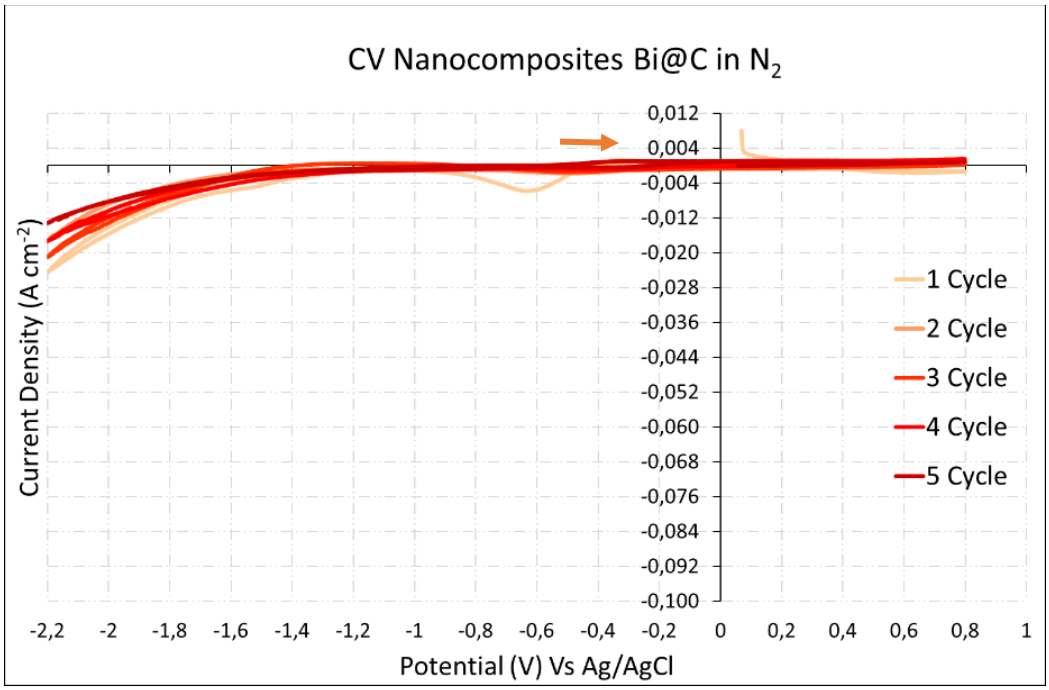

Graph 6 *CV of nanocomposites Bi@C.*

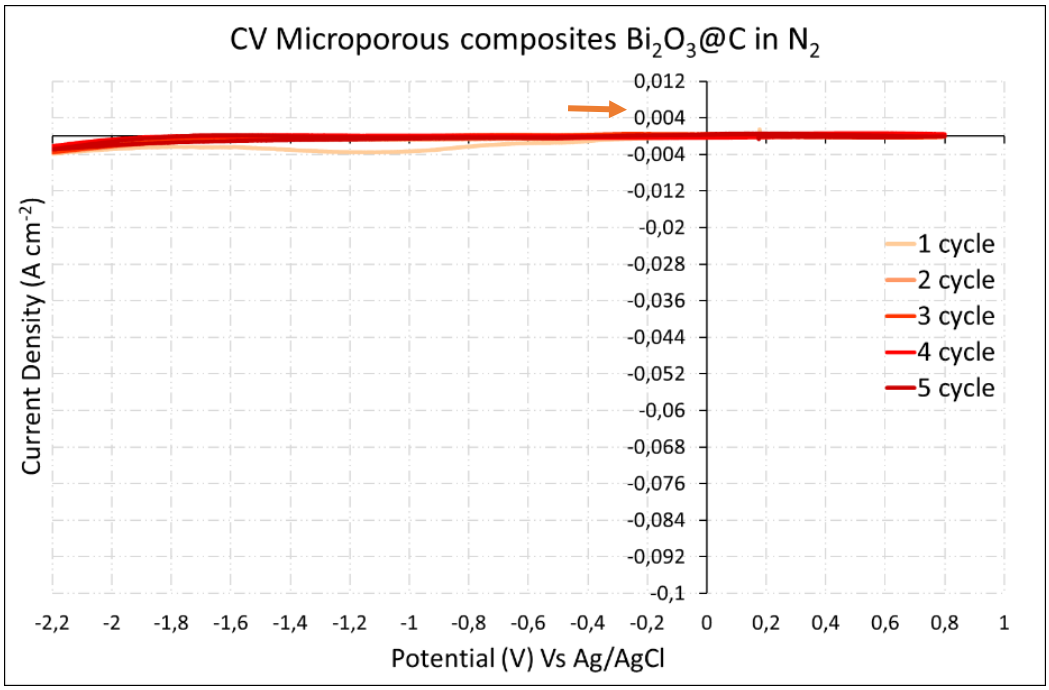

Graph 7 *CV of microp. composites Bi_2O_3@C.*

LSV analyses were performed in relation to the activity of the electrocatalysts in the previously observed CV potential range. Each catalyst was measured in a nitrogen and a carbon dioxide saturated atmosphere. All results are shown in Graph 8, 9, 10, 11, 12 and 13.

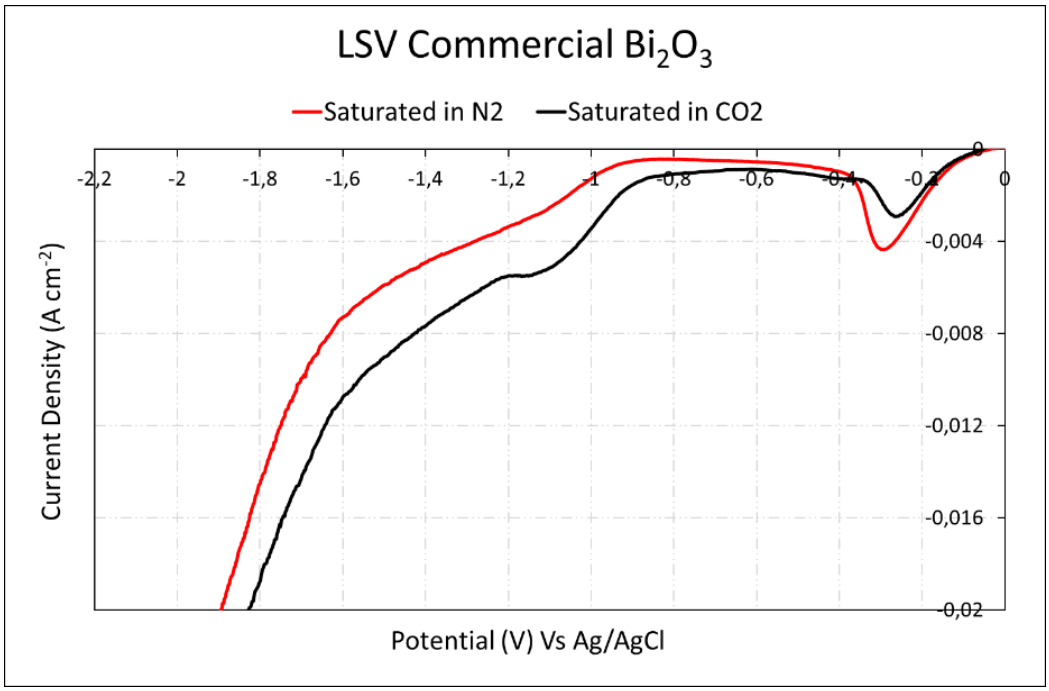

Graph 8 *LSV of commercial Bi_2O_3.*

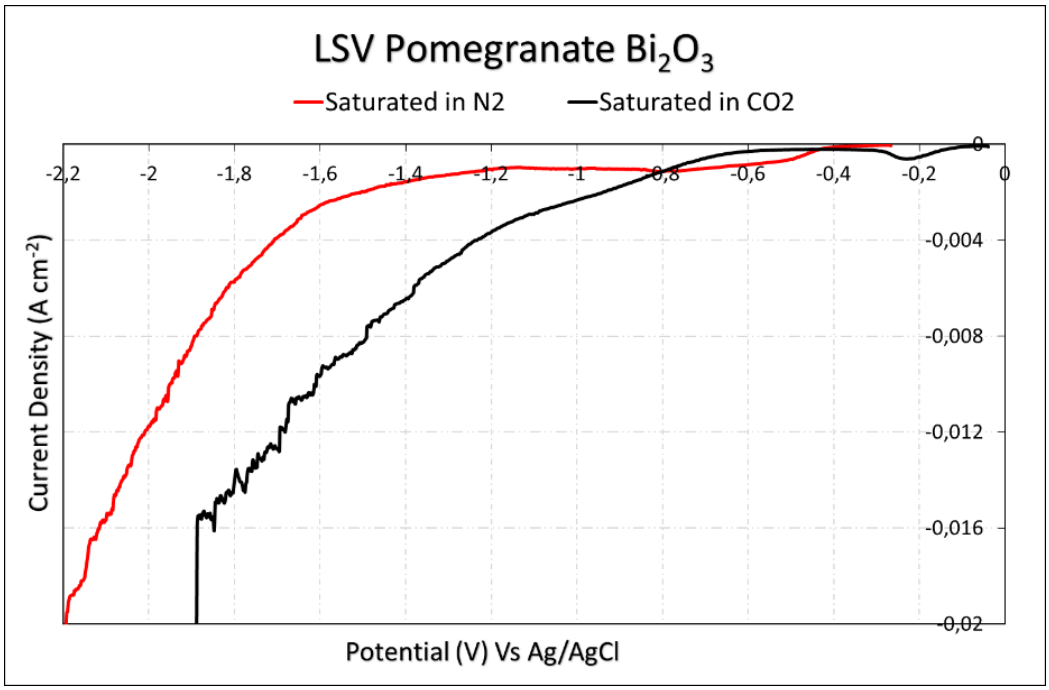

Graph 9 *LSV of pomegranate Bi_2O_3.*

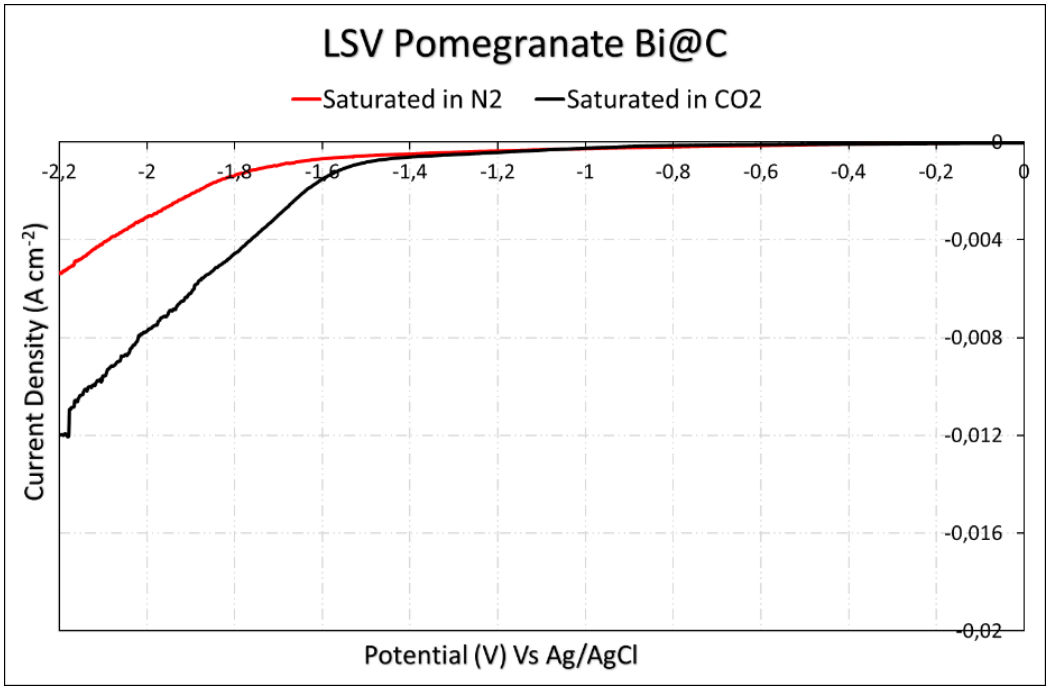

Graph 10 *LSV of pomegranate Bi@C.*

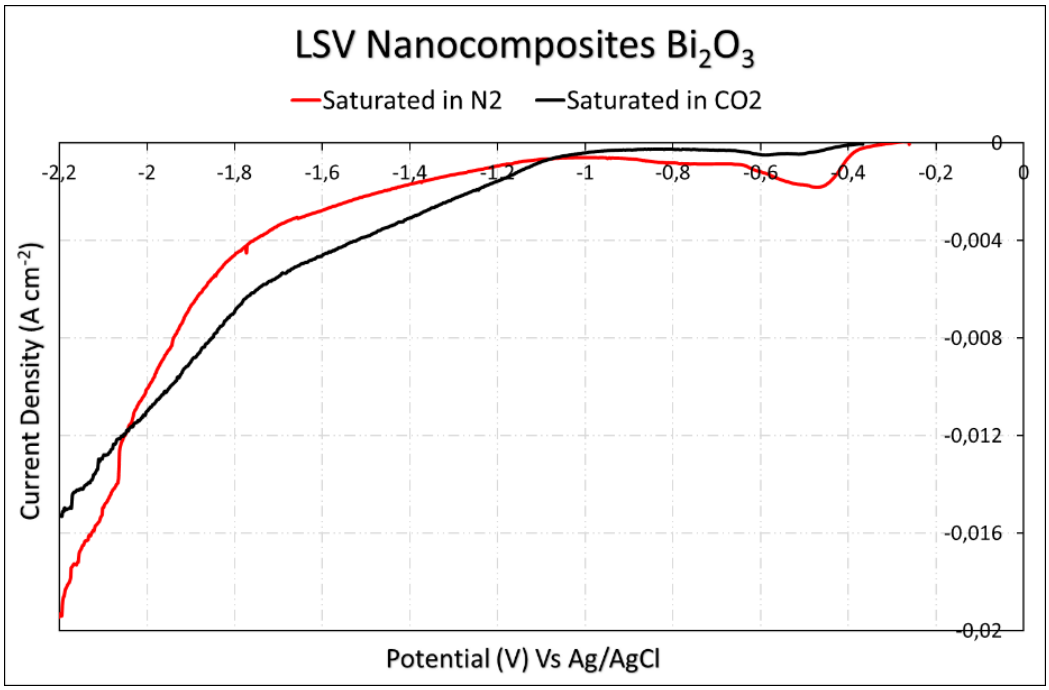

Graph 11 *LSV of nanocomposites Bi_2O_3.*

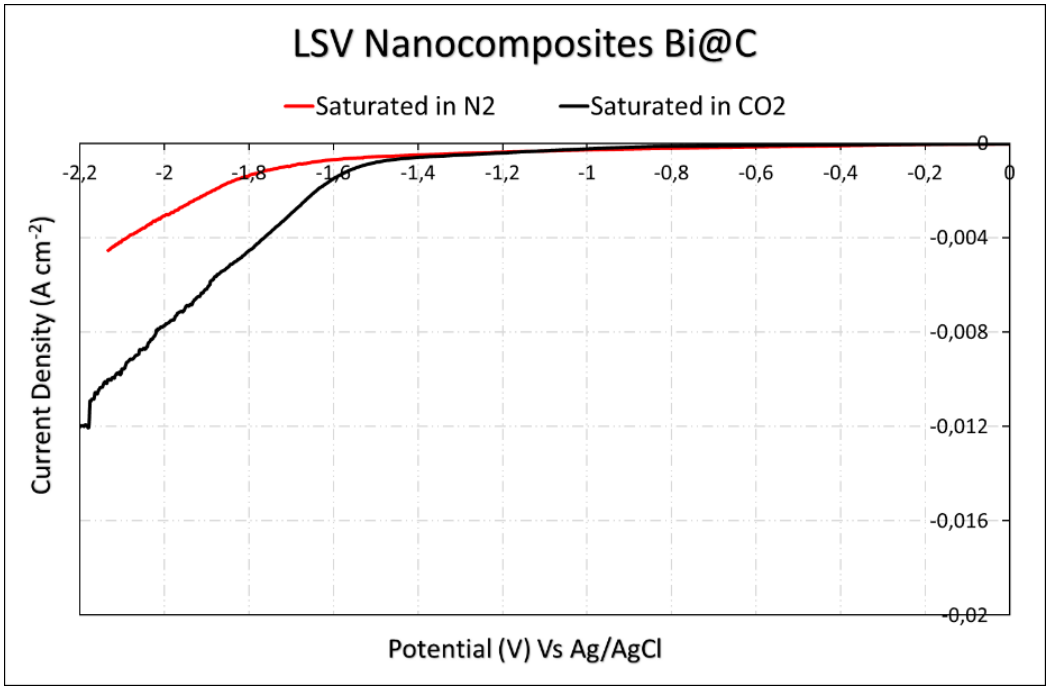

Graph 12 *LSV of nanocomposites Bi@C.*

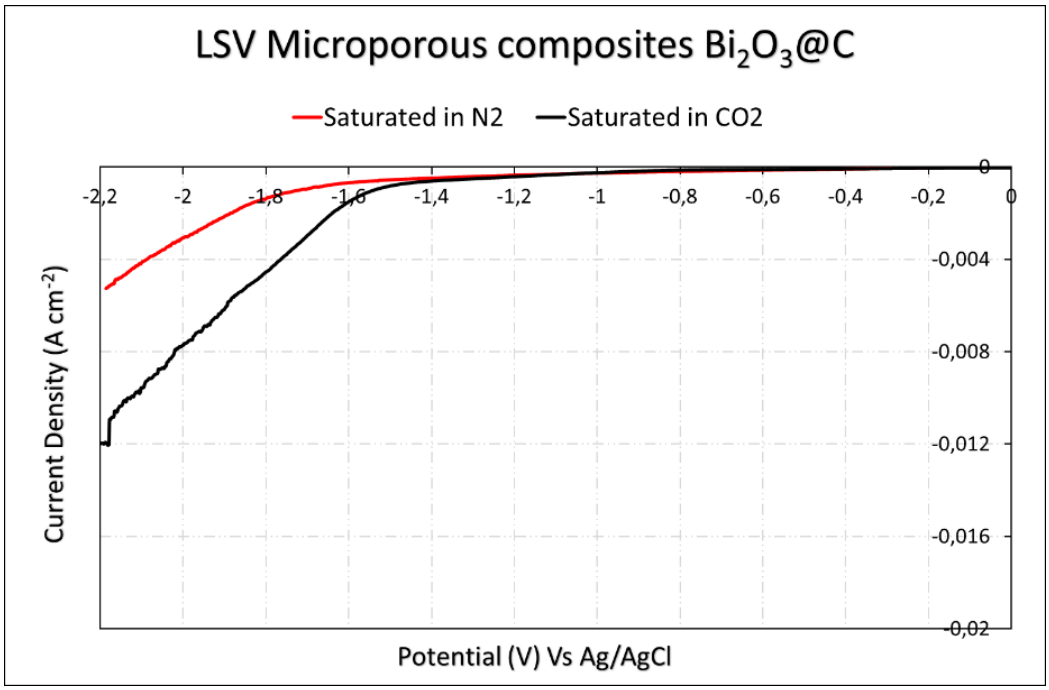

Graph 13 *LSV of microp. composites Bi_2O_3@C.*

For each catalyst the onset potential of the hydrogen evolution reaction is typically around -1,2 V vs Ag/AgCl, which is as expected from theory. When comparing for each catalyst the voltammogram based on the analysis on CO_2 saturated atmosphere vs the one in N_2 saturated atmosphere, it is possible to observe for the former a shift of the onset potential closer to zero, due to the CO_2 reduction reaction, which happens at different potentials than the hydrogen evolution reaction. Since commercial bismuth was used as a reference, in Graph 8 it is possible to observe a proper peak at -0,3 V vs Ag/AgCl probably caused by the reduction of the Bi_2O_3 catalyst, only partially reduced from the previous CV. In the same graph, an increase in current density can be observed in the potential range between -0,8 V and -1,2 V, which can probably be attributed to the CO_2 reduction reaction. In Graph 10, 12, and 13 relating to the pomegranate Bi@C, nanocomposites Bi@C and microp. composites Bi_2O_3@C carbon structures, the main difference between LSV in CO_2 and N_2 atmosphere lies in the onset potential, which is closer to zero in the second case due to the CO_2 reduction. In Graph 9 and 11 for the pomegranate Bi_2O_3 and nanocomposites Bi_2O_3 catalysts, a small current density can be observed even at low potential due to the partial reduction of the catalyst, thus the HER peak with an onset potential at -1,2 V for the red curve and -0,8 for the black one. In contrast, a carbon-based catalyst such as pomegranate Bi@C (Graph 10), nanocomposites Bi@C (Graph 12) and microporous composites Bi_2O_3@C (Graph 13) exhibit generally higher potential for both curves, perhaps due to

lower activity and higher energy demand by the system or due to the absence of reduction contribution of bismuth oxide to the measured current density. The most visible case is that of pomegranate Bi_2O_3, with an onset potential in both CO_2 and N_2 curves around -1,6 V, which could also evidence a low selectivity for CO_2 compared to H_2. The nanocomposites Bi@C, on the other hand, showed a better selectivity for CO_2 than the previous one, as the onset potential of the CO_2 saturated curve is sufficiently different from the other (-0,8 V vs -1,6V vs Ag/AgCl), implying a reduction potential for CO_2 disclose to the HER potential. The microporous composites Bi_2O_3@C catalyst, unlike the others, has a lower overall current density, indicating a possible low activity and selectivity of the catalyst.

It has been impossible to test catalyst mesop. nanochain due to incompatibility with the drop-casting method used to deposit the catalyst on the rotating glassy disk used as the working electrode.

The obtained information from these analyses can be helpful in interpreting performance results as much as the physiochemical characterization data.

It is important to consider the susceptibility of the system used, as this varies from the actual reactor used to test the catalysts, mostly in the way the CO_2 is supplied to the catalysts (dissolved in solution vs gaseous).

3. Back pressure optimization

To allow the system made by the reactor and all its components of which the catalyst used, to work at the best at 85 °C, the reactor pressure can be modified to allow better performance after long duration experiment as described in Chapter 1, Paragraph 2.5.2. The procedure adopted in this phase of work is described in Chapter 3, Paragraph 2.2.

The results are shown in Graphs 14, 15, 16 and 17. Graph 14, relative to the pressure value determination, illustrates for each valve set point, the dynamic pressure measured by the digital pressure indicator. A linear correlation was determined between valve setting and pressure reading, in the valve set point range between 9 and 4.

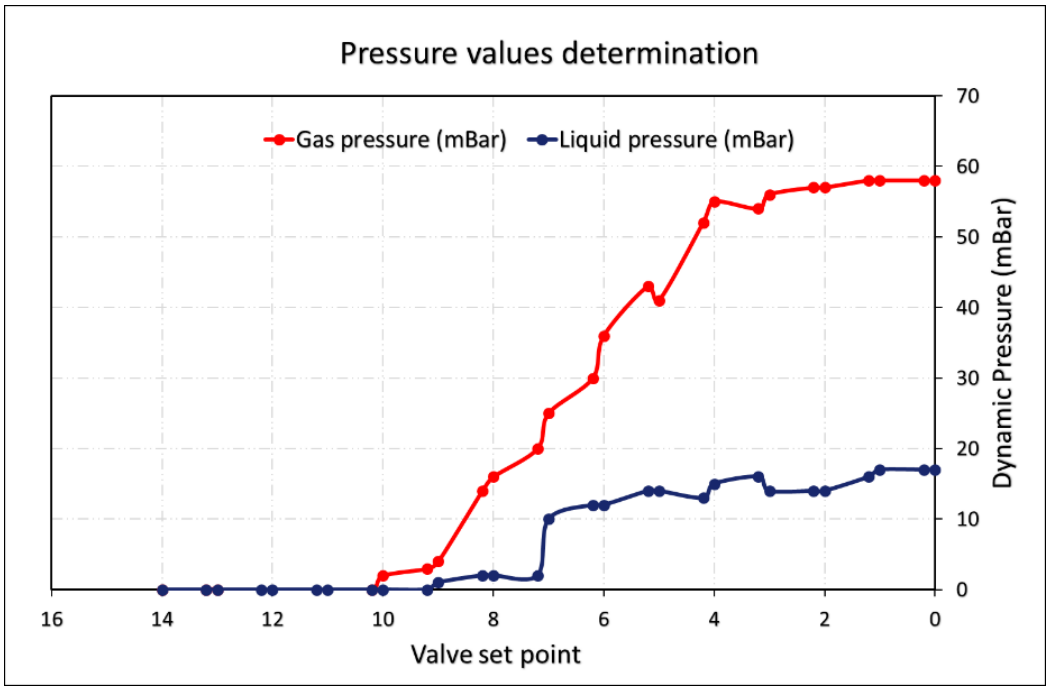

Graph 14 *Pressure values determination.*

Out of this range, pressure variations are probably too small to be detected by the pressure indicator, which displays similar constant values.

The results obtained from the chronopotentiometric measurement at different back pressures are illustrated in Graphs 15, 16 and 17. The valve set points used are shown in Table 8.

Table 8 *Correlation valve set point - pressure.*

Valve set point	Pressure (mBar)
5,10	40
5,0	41
4,15	48
3,10	59

Initial analyses were limited to the adopted pressure, to observe how the system would respond to changes, after which larger values were tested. In Graph 15, the results observed in terms of faradaic efficiency are similar for each pressure used, the system shows small fluctuations due to the temperature affecting the various components, as described earlier in Chapter 1, Paragraph 2.5.1.

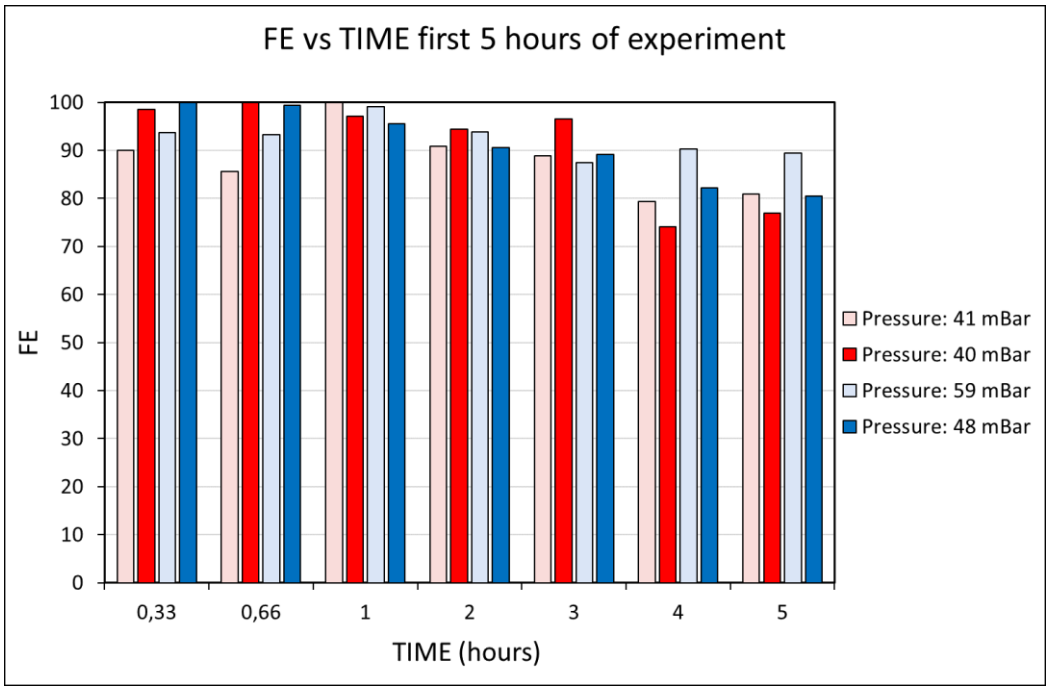

Graph 15 *Faradaic efficiency at different pressure values in the first 5 hours of chronopotentiometry test at -100 mA cm^{-2}.*

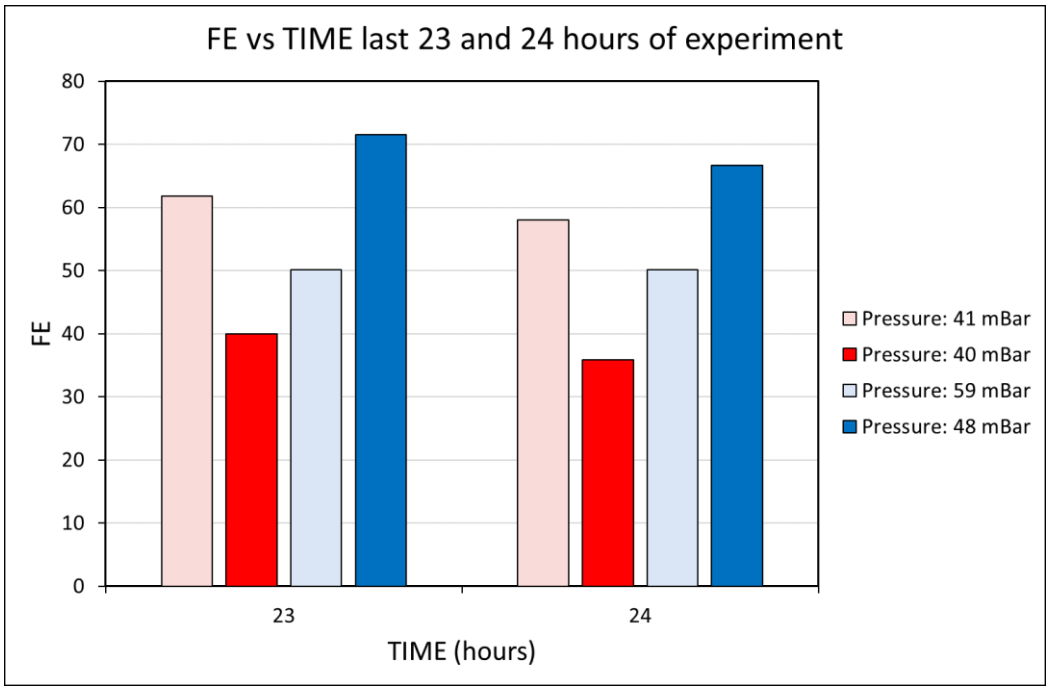

Graph 16 *Faradaic efficiency at different pressure values in the last 23 and 24 hours of chronopotentiometry test at -100 mA cm^{-2}.*

The data show a greater difference when a long measurement period is involved, as shown in Graph 16. After 23 and 24 hours of experiment, the back pressure adopted is a critical factor in maintaining high the faradic efficiency.

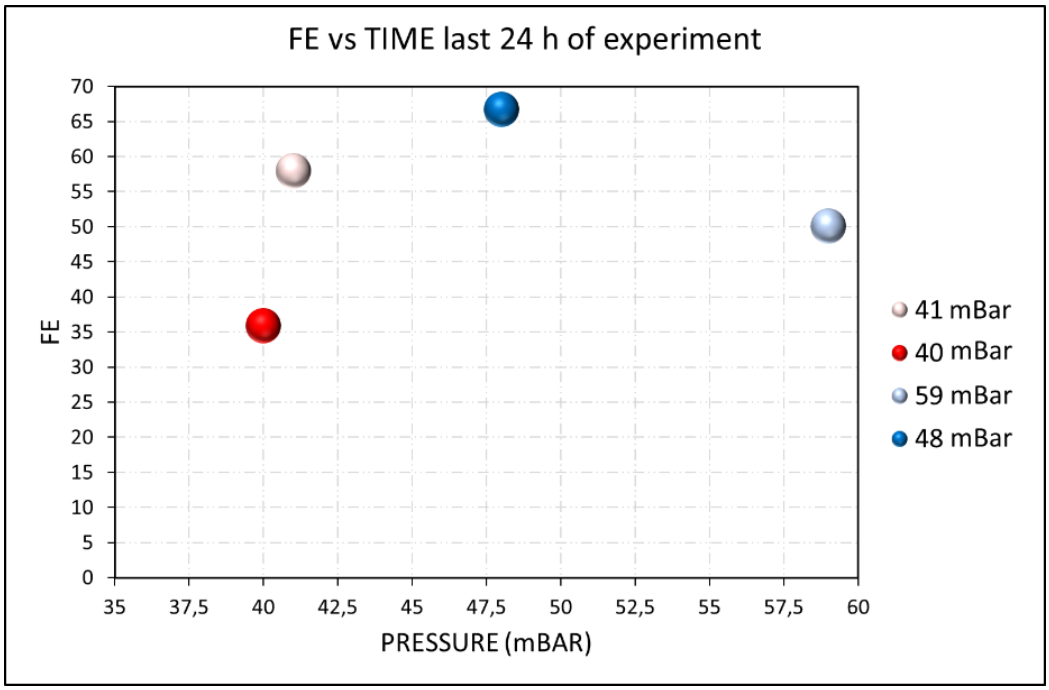

Graph 17 *Faradaic efficiency at different pressure values in the last 23 and 24 hours of chronopotentiometry test at -100 mA cm^{-2}.*

The same results are illustrated in Graph 17, which better illustrates the optimal pressure value at 48 mBar, to maintain the FE at the maximum value of 66,7.

Using a pressure lower or higher than 48 mBar, resulted in a reduction in faradaic efficiency probably due to flooding of the catholyte through the GDE in the first case, and to a structural overstress of the GDE in the second. These phenomena are probably difficult to highlight for short-term analyses, as observed in Graph 15, but more evident after a long period of time under pressure, as evident in Graph 16 and 17.

The optimal back pressure was used for subsequent analyses to determine the performance of the new catalyst series under the best reactor conditions.

4. ECSA determination

The ECSA measurement was performed at the optimal back pressure of 48 mBar and at 85 °C, using a catholyte reactor. The results are illustrated in Table 9. The linear regression obtained for each catalyst, after cyclovoltammetry at different scan rates, allowed to obtain the relative capacitance of each catalyst using the DCM method described in Chapter 3, Paragraph 5. The relative capacitance C_{DL} of each catalyst is shown in Table 9.

Table 9 *Capacitance values for the new series of catalysts*

Catalyst structure	C_{DL} (μF cm^{-2})	$C_{DL\ CAT.}$ / $C_{DL\ COMM\ Bi}$
Commercial Bi_2O_3	506	1
Pomegranate Bi_2O_3	575	1,14
Pomegranate Bi@C	1042	1,81
Nanocomposites Bi_2O_3	779	1,54
Nanocomposites Bi@C	623	1,23
Mesop. nanochain Bi@C	876	1,73
Microp. composites Bi_2O_3@C	890	1,76

The relative capacitance for each catalyst was obtained as described in Chapter 3 Paragraph 5.2, the ratio was calculated by normalization of each catalyst C_{DL} with the C_{DL} of commercial Bi_2O_3 used as a reference.

Analysing this data, the differences between the specific surface area and the electrochemical active is clear. In particular, the pomegranate Bi@C catalyst appears to have a larger active area than the microporous Bi_2O_3@C one, and also the nanocomposites Bi_2O_3 catalyst and mesop. nanochain Bi@C catalyst also appears to have a larger active area compared to the other catalysts instead of the specific one.

The reason why the electrochemically active surface area might have a different trend from the specific one, probably lies in the presence of the carbon particles and their distribution. From the ICP-MS analysis, it is observed that the mesop. nanochain Bi@C catalyst and the microp. composites Bi_2O_3@C catalyst, have a carbon percentage of 84,3% and 67%, respectively. The capacitance ratio results reported in Table 9, however, evidence their capacitance to be the highest after the pomegranate Bi@C catalyst among the other products. This result is interesting considering that amorphous carbon microparticles should have a higher electrical resistivity than bismuth, which is 106,8 μΩ cm. Instead, a better activity is observed by the capacitance determination for the three catalysts of the series with the highest carbon concentration and the lowest bismuth concentration. As previously mentioned, the results must be interpreted considering the shape, morphology and carbon distribution of the catalyst,

as a key factor in their conductivity and activity. Overall, although there are small differences among the catalysts, they all showed similar capacitance, which will allow conclusions on behalf of their performance, considering the previous information regarding their electrochemical activity and physical characterization.

In conclusion, the synthesized products showed different characteristics in terms of specific and electrochemical active surface area, this phenomenon is caused by several factors such as the bismuth and carbon concentration, and their shape and distribution. However, with small differences, all catalysts showed similar values, which suggests that even catalysts with low specific surface area, such as the nanocomposites Bi_2O_3 catalyst, may perform better than expected based on previous analyses.

5. Chronopotentiometry measurements

The chronopotentiometry test's results are shown in this section in graphs 18, 19 and 20, the graphs illustrate the catalysts performances at the first, second and third levels of analysis, respectively.

The first level results were obtained by testing the new series of catalysts at different current densities i.e. at -50, -75, -100, -125, and -150 mA cm^{-2} to observe how the carbon integrated catalysts, behave compared to the others.

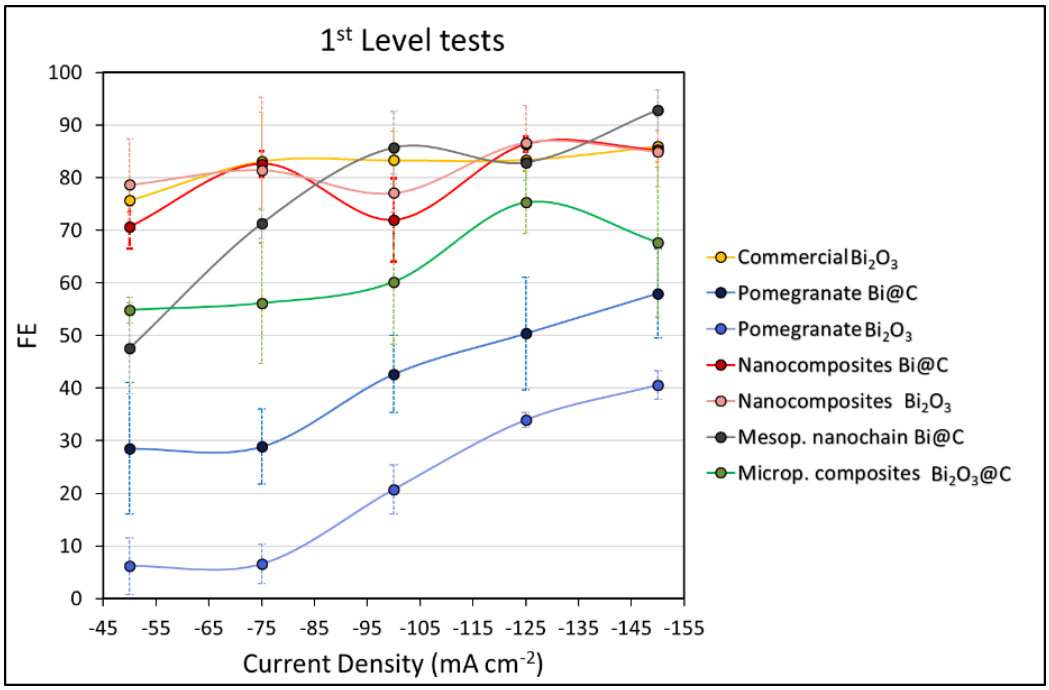

Graph 18 *First level measurement, Current density Vs Faradaic efficiency.*

Observing Graph 18, it is clear that two catalysts such as pomegranate Bi_2O_3 and Bi@C, perform poorly at every current density analysed. The microp. composites Bi_2O_3@C catalyst seems to have an increasing faradaic efficiency with the increase of current density with a maximum value of 75,3% at -125 mA cm^{-2}. The other four catalysts have similar values of FE, but small differences can be seen, as the commercial Bi_2O_3 catalyst seems to have a very steady trend, while the mesop. nanochain Bi@C catalyst perform better at higher current density.

The nanocomposites Bi_2O_3 and Bi@C catalysts seem to have a very similar trend at every current density measured.

Differences in the catalyst's performance at different current densities can be attributed to several factors, such as morphology, which may require an energy demand greater to enable the electron transfer from the bismuth particle within the crystalline structure to the substrate, the conductivity of the catalyst which depends mostly by its constituents, the chemical structure, which is still highly discussed in terms of better performances from an oxidized or metallic structure and surely the structural stability of the catalyst. Faradaic efficiency usually decreases at higher current density because of the electrowetting and the degradation of the catalyst particles under high current stress.

The first level measurement proved that the pomegranate Bi_2O_3, the pomegranate Bi@C and the microp. composites Bi_2O_3@C catalysts, did not perform well compared to commercial bismuth at any current density, while the other catalysts performed better and more similar to the reference. However, it is also possible to conclude that none of the analysed catalysts showed any signs of degradation behaviour or loss of faradaic efficiency by increasing the current density, mostly because of the short length of the experiment.

Since the obtained results are insufficient to determine the structural stability and efficiency of the new catalyst series, each product was subjected to the second level test for 6 hours at -100 mA cm^{-2}. As in the first level, the second level measurement consisted of three GDEs of each catalyst tested; the values shown in Graphs 18 and 19 are obtained from the average of the three measurements, and the error bars were added after calculating the standard deviation of each point. Graph 19, shows the results obtained for each catalyst in second level measurement.

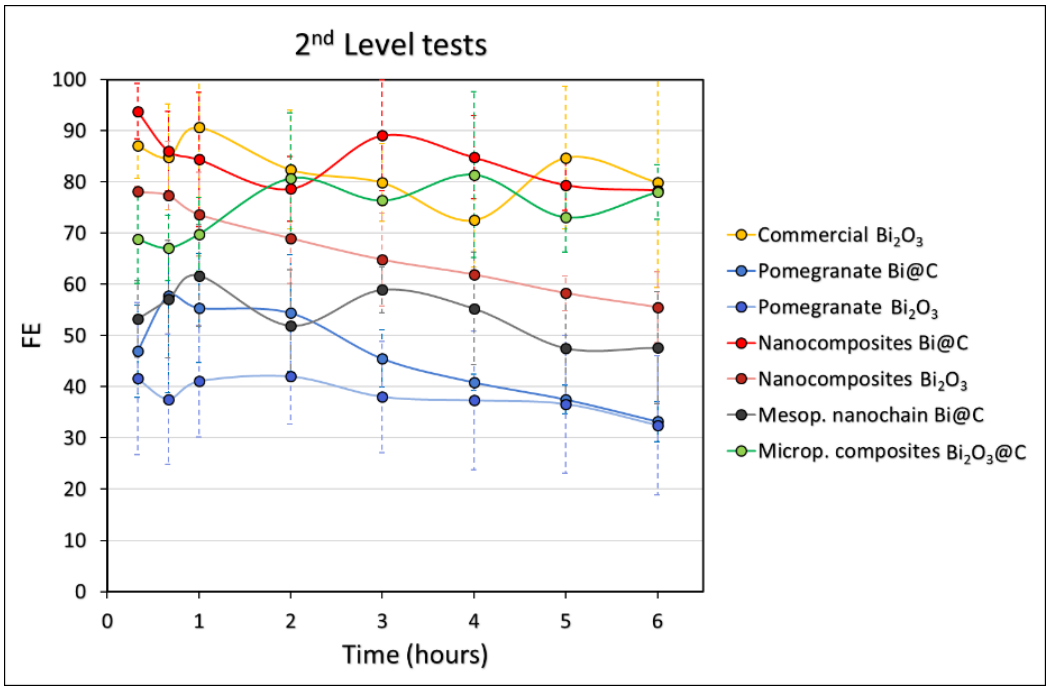

Graph 19 *Second level measurement, Faradaic efficiency for a chrono potentiometric measurement at -100 mA/cm², for 6 hours, for different catalysts.*

The pomegranate Bi_2O_3 and Bi@C catalysts showed the worst performance compared to the others in terms of FE. After 6 hours of measurement, it is evident that also the mesop. nanochain Bi@C catalyst and the nanocomposites Bi_2O_3 catalyst, performed badly. In particular, the former performed poorly from the first hour of measurement with an overall FE always under 60%, while the latter showed a decreasing FE, with low FE after two hours of measurement. The nanocomposites Bi@C catalyst, showed a good efficiency of about 95% at the beginning with a decreasing trend to an FE of about 80% after 6 hours. On the contrary, catalyst microp. composites Bi_2O_3@C showed an increasing trend in efficiency, going from an FE of about 70% at the beginning and going steady to an FE of about 80% after 6 hours. The commercial Bi_2O_3 used as a reference showed an oscillating but mostly steady trend on the same value of FE, starting from 87% and reaching 79% after 6 hours.

Considering the mean total cell potential observed during the second level test for each catalyst shown in Table 10, it is possible to observe that all the synthesized catalysts do not have an energy demand particularly high.

Table 10 *Mean total cell potential observed for the chatolyte flow-by reactor during 6 hours experiment at -100 mA cm^{-2} current density, at 85 °C and at 48 mBar of back pressure.*

Catalyst structure	Mean total cell potential during 6 hours experiment
Commercial bismuth	-4,71 V Vs Ag/AgCl
Pomegranate Bi_2O_3	-4,16 V Vs Ag/AgCl
Pomegranate Bi@C	-4,84 V Vs Ag/AgCl
Nanocomposites Bi_2O_3	-4,16 V Vs Ag/AgCl
Nanocomposites Bi@C	-4,98 V Vs Ag/AgCl
Mesop. Nanochain Bi@C	-3,51 V Vs Ag/AgCl
Microp. composites Bi_2O_3@C	-4,13 V Vs Ag/AgCl

The last three catalysts described followed the third level test based on their better results respect to the others, which already manifested low faradaic efficiency after 6 hours at -100 mA cm^{-2} of current density. Graph 20 shows the results of the 24-hours chronopotentiometry tests.

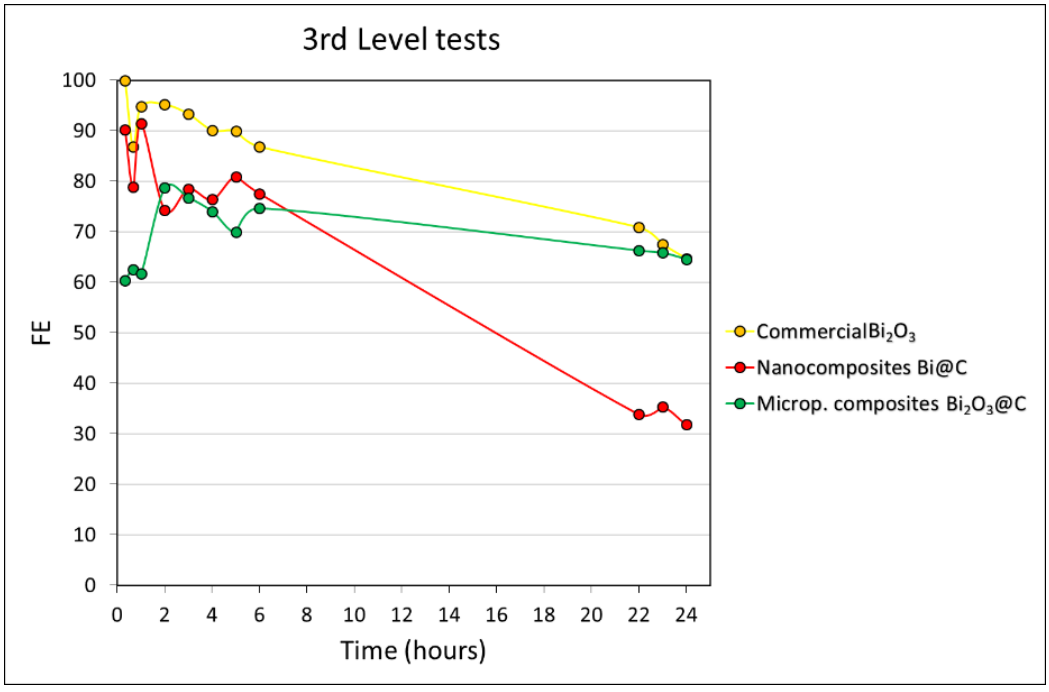

Graph 20 *Third level measurement, Faradaic efficiency for a chrono potentiometric measurement at -100 mA/cm^2, for 24 hours, for different catalysts.*

The three catalysts, of which the commercial Bi_2O_3 did not belong to the new synthesised series, but was used as a reference, showed different trends.

Commercial bismuth was the catalyst with the highest FE at the beginning of the experiment, with a decreasing trend. The nanocomposites Bi@C catalyst has a high

faradaic efficiency at the start, but reaches a low FE after 22 hours, going from 90% of FE to 33,8% after 22 hours, and ultimately to 31,8% after 24 hours of experiment.
In contrast, the microp. composites Bi_2O_3@C catalyst started the test showing poor efficiency compared to the other two catalysts tested, with an initial FE value of about 60,42%. However, it manifested an increasing trend reaching 74% FE after two hours, and steadily descending to 66% after 22 hours and 64% after 24 hours, reaching the same FE as commercial Bi_2O_3, after 24 hours of testing.
The obtained results obtained can be interpreted according to the percentage and carbon distribution of the two catalyst tested. A percentage of 89,6% of bismuth and 10,4% of carbon was observed in catalyst nanocomposites Bi@C, whereas only 33% of bismuth and 67% of carbon was determined for the microporous Bi_2O_3@C catalyst. A higher concentration of bismuth such as in the nanocomposites Bi@C catalyst, could explain the high FE observed in all three levels of measurement and in particular in the third one (Graph 20), which is very similar to commercial Bi_2O_3. Carbon is in fact selective for the production of hydrogen from the catholyte solution, decreasing the overall selectivity of the catalyst, a phenomenon that could explain the lower selectivity of the microp. composites Bi_2O_3@C catalyst. Observing Graphs 12 and 13 in Chapter 4 Paragraph 2, similar behaviour was expected. The nanocomposites Bi@C showed an onset potential for the hydrogen evolution reaction in a nitrogen-saturated solution at -1,6 V Vs Ag/AgCl (Graph 12) and at -0,8 V Vs Ag/AgCl in a CO_2-saturated solution while the microp. composites Bi_2O_3@C catalyst showed an onset potential for the red curve at -1,2 V Vs Ag/AgCl and -1,0 V Vs Ag/AgCl for the black one (Graph 13), demonstrating a closer potential window between the CO_2 reduction and the HER, suggesting a lower selectivity of the catalyst. Judging from SEM-EDS images 3 and 5 in Chapter 4 Paragraph 1.2, the nanocomposites Bi@C catalyst has a very homogenous carbon distribution around the bismuth particles, while the microp. composites Bi_2O_3@C catalyst has a structure in which the carbon particles are separated and placed among the bismuth ones. In the first case, the morphology of the microstructure could be the cause of the decreasing FE trend observed in Graph 20. On the contrary, in the second case, the carbon particles placed between those of bismuth could lead to a lower overall FE, caused by the large percentage of carbon occupying the total specific surface area available on the catalyst, and which can interact with the catholyte leading to HER. However, the structural morphology may provide better structural stability than the nanocomposites Bi@C catalyst, which was

observed to achieve poor results after 22 hours of measurement, probably due to the sintering of the microparticles catalyst.

Furthermore, the behaviour observed for the microp. composites Bi_2O_3@C catalyst, at the beginning of the analysis, could be explained by considering a structural rearrangement of the carbon microparticles. In Graphs 19 and 20, it is evident the increase in faradaic efficiency for the catalyst after 2 hours under -100 mA cm^{-2} at 85 °C, one interpretation of this phenomenon can be the partial activation of the catalyst, by the sintering of the carbon particles after few hours under these conditions. Carbon particles aggregating between them self, decrease their surface area, leading to a reduction in HER, and subsequently allow the exposure of a larger bismuth surface, leading to an increase in FE.

In conclusion, the chronopotentiometry tests provided important information on the actual behaviour of the new series of bismuth-based catalyst, which can be correlated with the information obtained from the characterization analyses to predict and study their behaviour on the electrochemical CO_2 reduction at 85°C.

Chapter 5
Conclusion

In the last chapter of this work, the conclusion on this project will be provided based on the results obtained from the several analyses performed.

1. Conclusion on the new bismuth-based electrocatalysts.

The syntheses and analyses performed during this work, have provided information about the new synthesised series of Bi-based electrocatalysts, integrated with carbon microparticles to better resist thermal and electric stress, to catalyse the CO_2 electroreduction to formic acid at 85 °C and a current density of -100 mA cm^{-2}.

The physiochemical and electrochemical characterization provided several data used to interpret the behaviour of each catalyst in the performance testing phase of this work.

The catholyte reactor used in this work has been optimized in terms of pressure conditions used for the chronopotentiometry measurement, to ensure the best structural stability of the GDE in relation to the pressure and temperature conditions.

Several factors play a key role in the electrocatalysis of CO_2, besides the reactor condition of pressure, temperature and current density supplied, such as the selectivity, structural stability and activity of the catalyst used. The new synthesized series of electrocatalysts have different bismuth and carbon concentrations, resulting in different faradaic efficiency, electrochemical surface area, shape and morphology of the catalyst. The specific surface area is also influenced by the distribution and shape of the carbon-integrated microparticles in the structure. In this work, similarities were found between the new bismuth-based electrocatalysts, and the tin product from the original synthesis in terms of physical characteristics, indicating a close behaviour between tin and bismuth under hydrothermal synthesis. On the contrary, XRD data showed several differences between these two elements, such as the tendency of bismuth to reduce at high temperature and high pressure from Bi^{3+} to Bi^{0}, and its stability to remain in this oxidation state under normal conditions, while tin was observed to tend to easily re-oxidise to Sn^{4+} under atmosphere condition. CV and LSV analyses, provided important results regarding the electrochemical behaviour of the synthesized catalyst under air and CO_2 conditions, showing the potential region of their activity. The ECSA analysis gave evidence of the electroconductivity and relative capacitance of each catalyst, leading to knowledge of the difference between the previously observed specific surface area and the electrochemical active one.

The chonopotentiometry tests performed at 85 °C in a catholyte flow-by reactor with an optimal back pressure of 48 mBar, allowed the determination of the catalyst's efficiency at several current densities and duration of the experiment.

The results showed catalyst nanocomposites Bi@C and microp. composites Bi_2O_3@C as the most promising of the series, based on their stability and selectivity at the different current densities studied and after the different measurement times. The pattern followed by the catalysts in terms of faradaic efficiency and oxidation state was not clear from this work; further analyses need to be performed to better understand why oxidised and metal catalysts work differently. However, it was possible to conclude that the catalyst with a sufficiently large specific surface area and a sufficiently high electrochemical active surface area compared to the others, performed best. It was possible to interpret the trend in the faradaic efficiency over the 24-hour measurement period, based on the shape and microstructural morphology observed and in relation to the chemical composition of the bismuth and carbon percentage.

In summary, this work provided a new series of electrocatalyst structured with bismuth microparticles integrated with carbon and several information on their performances. Differences and similarities with the original tin-based version electrocatalysts were highlighted. The reactor set-up was optimized to perform for maximum faradaic efficiency. Two electrocatalysts proved to be the best performing and most promising, such as the nanocomposites Bi@C catalyst and the microporous composites Bi_2O_3@C catalyst after short-term and long-term experiments, compared to the others.

Further analyses can be conducted to optimize and determine the performance of the catalysts, especially the microporous composites Bi_2O_3@C catalyst, to study its stability at a current density above -100 mA cm^{-2}, and chronopotentiometry experiment with longer duration than twenty-four hours.

Bibliography

[1] I. Ghiat and T. Al-Ansari, Review of carbon capture and utilization as a CO_2 abatement opportunity within the EWF nexus, College of science engineering, Qatar 2021.

[2] M. Duarte, Development of electrochemical reactors for CO_2 electrolysis, ELCAT, Antwerp 2022.

[3] B. de Mont, Engineering aspects for the electrochemical CO_2 reduction to formate, ELCAT, Antwerp 2022.

[4] P. Duarah, D. Haldar, V. Yadav, and M. K. Purkait, Progress in the electrochemical reduction of CO_2 to formic acid: A review on current trends and future prospects, Indian institute of technology, India 2021.

[5] K. Yang, R. Kas, W. A. Smith and T. Burdyny, Role of the carbon-Based gas diffusion layer on flooding in a gas diffusion electrode cell for electrochemical CO_2 reduction, ACS Energy Lett. 2021, 6, 33−40.

[6] A. Löwe, C. Rieg, T. Hierlemann, N. Salas, D. Kopljar, N. Wagner and E. Klemm, Influence of temperature on the performance of gas diffusion electrodes in the CO_2 reduction reaction, Institute of Chemical Technology, University of Stuttgart, Germany 2019.

[7] Ullmann's Encyclopedia of Industrial Chemistry - 2016 - Hietala - Formic Acid.

[8] F.Yu, K. Deng, M. Du, W. Wang, F. Liu and D. Liang, Electrochemical CO_2 reduction: from catalysts to reactive thermodynamics and kinetics, Carbon Capture Science & Technology, Volume 6, 2023.

[9] SF Qin, YJ Xie, Yi Wang, Le-Xing You, JH Fang and JJ Sun, Fundamentals on kinetics of electrochemical reduction of CO_2 at a bismuth electrode, Journal of Electroanalytical Chemistry, Volume 904, 2022.

[10] H. Yang, J. J. Kaczur, S. D. Sajjad and R. I. Masel, Journal of CO_2 Utilization, Volume 42, 2020.

[11] Z. Yang, F. E. Oropeza and K. H. L. Zhang, P-block metal-based (Sn, In, Bi, Pb) electrocatalysts for selective reduction of CO_2 to formate, APL Mater. 8, 2020.

[12] Stefan Ringe, Ezra L. Clark, Joaquin Resasco, Amber Walton, Brian Seger, Alexis T. Bell, and Karen Chan, Understanding cation effects in electrochemical CO_2 reduction, Energy Environ. Sci., 2019, 12, 3001.

[13] B. Hammer, J.K. Norskov, Why gold is the noblest of all the metals, Centre for Atomic-scale Materials Physics, Physics Department, Technical University of Denmark, Nature, Vol 376, 20 July 1995.

[14] J.E. Pander, III, M. F. Baruch, and A. B. Bocarsly, Probing the mechanism of aqueous CO_2 reduction on post-transition-metal electrodes using ATR-IR spectroelectrochemistry, Department of Chemistry, Princeton University, Princeton, New Jersey 08544, United States, 2016.

[15] P. Deng, H. Wang, R. Qi, J. Zhu, S.Chen, F. Yang, L. Zhou, Kai Qi, H. Liu, and B. Yu Xia, Bismuth oxides with enhanced bismuth−oxygen structure for efficient electrochemical reduction of carbon dioxide to formate, ACS Catal. 2020, 10, 743−750, 2019.

[16] X. An, S. Li, X. Hao, X. Du, T. Yu, Z. Wang, X. Hao, A. Abudulaa and G. Guan, The in situ morphology transformation of bismuth based catalysts for the effective electroreduction of carbon dioxide, Sustainable Energy Fuels, 2020, 4, 2831, 2020.

[17] P. Sivasubramanian, Jih-Hsing Chang, S. Nagendran, Cheng-Di Dong, Mohd Shkir and M. Kumar, A review on bismuth-based nanocomposites for energy and environmental applications, Chemosphere, Volume 307, Part 1, 2022.

[18] V. P. Zhukov, V. M. Zhukovskii, V. M. Zainullina, and N. I. Medvedeva, Electronic structure and chemical bonding in bismuth sesquioxide polymorphs, Journal of structural chemistry, Vol. 40, No. 6, 1999.

[19] Y. Hori, H. Wakebe, T. Tsukamoto and O. Koga, Electrocatalytic process of CO selectivity in electrochemical reduction of CO_2 at metal electrodes in aqueous media,1993.

[20] Yong X. Gan, Ahalapitiya H. Jayatissa, Zhen Yu, Xi Chen, and Mingheng Li, Hydrothermal Synthesis of Nanomaterials, Journal of Nanomaterials Volume 2020.

[21] K. S. W. Sing, D. H. Everett, R. A. W. Haul, L. Moscou, R. A. Pierotti, J. Roquerol, and T. Siemieniewska Pure Appl. Chem. 57, 603 (1985).

[22] Paula Connor*, Jona Schuch, Bernhard Kaiser and Wolfram Jaegermann, The Determination of Electrochemical Active Surface Area and Specific Capacity Revisited for the System MnOx as an Oxygen Evolution Catalyst, Z. Phys. Chem. 2020; 234(5): 979–994.

[23] WeiWei Wena, Mingzhong Zoua, Qian Fenga, Jiaxin Lia,b, Lunhui Guanb, Heng Laia, Zhigao Huanga, Cu particles decorated pomegranate-structured SnO_2@C composites as anode for lithium ion batteries with enhanced performance, Electrochimica Acta 182 (2015) 272–279.

[24] Huijun Wang, Guowei Jiang, Xiangjun Tan, Junke Liao, Xia Yang∗, Ruo Yuan, Yaqin Chai, Simple preparation of SnO_2/C nanocomposites for lithium ion battery anode, Inorganic Chemistry Communications 95 (2018) 67–72.

[25] Wenjun Zhang, Songyuan Yang, Minghang Jiang, Yi Hu, Chaoquan Hu, Xiaoli Zhang, and Zhong Jin, Nanocapillarity and Nanoconfinement Effects of Pipet-like Bismuth@Carbon Nanotubes for Highly Efficient Electrocatalytic CO_2 Reduction, Nano Lett. 2021, 21, 2650−2657.

[26] Guoen Luoa, Weijian Liua, Songshan Zengb, Congcong Zhanga, Xiaoyuan Yua, Yueping Fanga, Luyi Sun, Hierarchal mesoporous SnO_2@C@TiO_2 nanochains for anode material of lithium-ion batteries with excellent cycling stability, Electrochimica Acta 184 (2015) 219–225.

[27] Ming-Shan Wang, Ming Lei, Zhi-Qiang Wang, Xing Zhao, Jun Xu, Wei Yang, Yun Huang, Xing Li, Scalable preparation of porous micron-SnO_2/C composites as high performance anode material for lithium ion battery, Journal of Power Sources 309 (2016) 238-244.

[28] Wenchao Ma, Shunji Xie, Xia-Guang Zhang, Fanfei Sun, Jincan Kang, Zheng Jiang, Qinghong Zhang, De-Yin Wu & Ye Wang, Promoting electrocatalytic CO_2 reduction to formate via sulfur-boosting water activation on indium surfaces, Nature Communications volume 10, Article number: 892 (2019).

[29] Critical Raw Materials Resilience: Charting a Path towards greater Security and Sustainability, European Commission, 2020.

[30] Christopher Batchelor-McAuley, E. Ktelhçn, E. O. Barnes, R. G. Compton, E. Laborda, and A. Molina, Recent Advances in Voltammetry, ChemistryOpen 2015, 4, 224 – 260, DOI: 10.1002/open.201500042.

[31] V. Vivier, A. Re´gis, G. Sagon, J.-Y. Nedelec, L.T. Yu, C. Cachet-Vivier, Cyclic voltammetry study of bismuth oxide Bi_2O_3 powder by means of a cavity microelectrode coupled with Raman microspectrometry, Electrochimica Acta 46 (2001) 907–914.

[32] Allen J. Bard Larry R. Faulkner, electrochemical methods fundamentals and applications, 1 (800)-CALL-WILEY (225-5945), 2001.

[33] N. Elgrishi, K. J. Rountree, B. D. McCarthy, E. S. Rountree, T. T. Eisenhart, and J. L. Dempsey, A Practical Beginner's Guide to Cyclic Voltammetry, Department of Chemistry, University of North Carolina, Chapel Hill, North Carolina 27599-3290, United States.

[34] R. Aldaco, I. Butnar, M. Margallo, J. Laso, M. Rumayor, A. Dominguez-Ramos, A. Irabien, P. E. Dodds, Bringing value to the chemical industry from capture, storage and use of CO_2: A dynamic LCA of formic acid production, Science of the Total Environment 663 (2019) 738–753.

[35] Alexander R. Heenan, Johan Hamonnet, and Aaron T. Marshall, Why Careful iR Compensation and Reporting of Electrode Potentials Are Critical for the CO2 Reduction Reaction, ACS Energy Lett. 2022, 7, 2357−2361.

[36] Y. X. Gan , A. H. Jayatissa, Z. Yu, Xi Chen , and Mingheng Li, Hydrothermal Synthesis of Nanomaterials, Volume 2020, Article ID 8917013, 3 pages https://doi.org/10.1155/2020/8917013.

[37] Weiran Zheng, iR Compensation for Electrocatalysis Studies: Considerations and Recommendations, ACS Energy Lett. 2023, 8, 1952−1958.

[38] S. M. Sze, Kwok K. Ng, Physics of Semiconductor Devices, A JOHN WILEY & SONS, JNC., PUBLICATION.

[39] Marcel Pourbaix, Atlas of Electrochemical Equilibria in - Aqueous Solutions, First English Edition 1966.

[40] Xiaole Jiang, Le Lin, Youwen Rong, Rongtan Li, Qike Jiang, Y. Yang, and Dunfeng Gao, Boosting CO_2 electroreduction to formate via bismuth oxide clusters, https://doi.org/10.1007/s12274-022-5073-0.

[41] Jing Wang, Jiating Mao, Xiaoli Zheng, Yannan Zhou, Qun Xu, Sulfur boosting CO_2 reduction activity of bismuth subcarbonate nanosheets via promoting proton-coupled electron transfer, Applied Surface Science 562 (2021) 150197.

[42] Ying Chuan Tan, Wei Kang Quek, Beomil Kim, Sigit Sugiarto, Jihun Oh, and Dan Kai, Pitfalls and Protocols: Evaluating Catalysts for CO_2 Reduction in Electrolyzers Based on Gas Diffusion Electrodes, ACS Energy Lett. 2022, 7, 2012−2023.

[43] Rafaël E. Vos and Marc T. M. Koper, The Effect of Temperature on the Cation-Promoted Electrochemical CO_2 Reduction on Gold, doi.org/10.1002/celc.202200239.

Webliography

[a] THE NOAA ANNUAL GREENHOUSE GAS INDEX (AGGI), updated spring 2023, https://gml.noaa.gov/aggi/aggi.html

[b] Un green deal europeo, https://commission.europa.eu/strategy-and-policy/priorities-2019-2024/european-green-deal_it

[c] Horizon Europe, https://commission.europa.eu/funding-tenders/find-funding/eu-funding-programmes/horizon-europe_en

[d] https://iupac.org/what-we-do/periodic-table-of-elements/